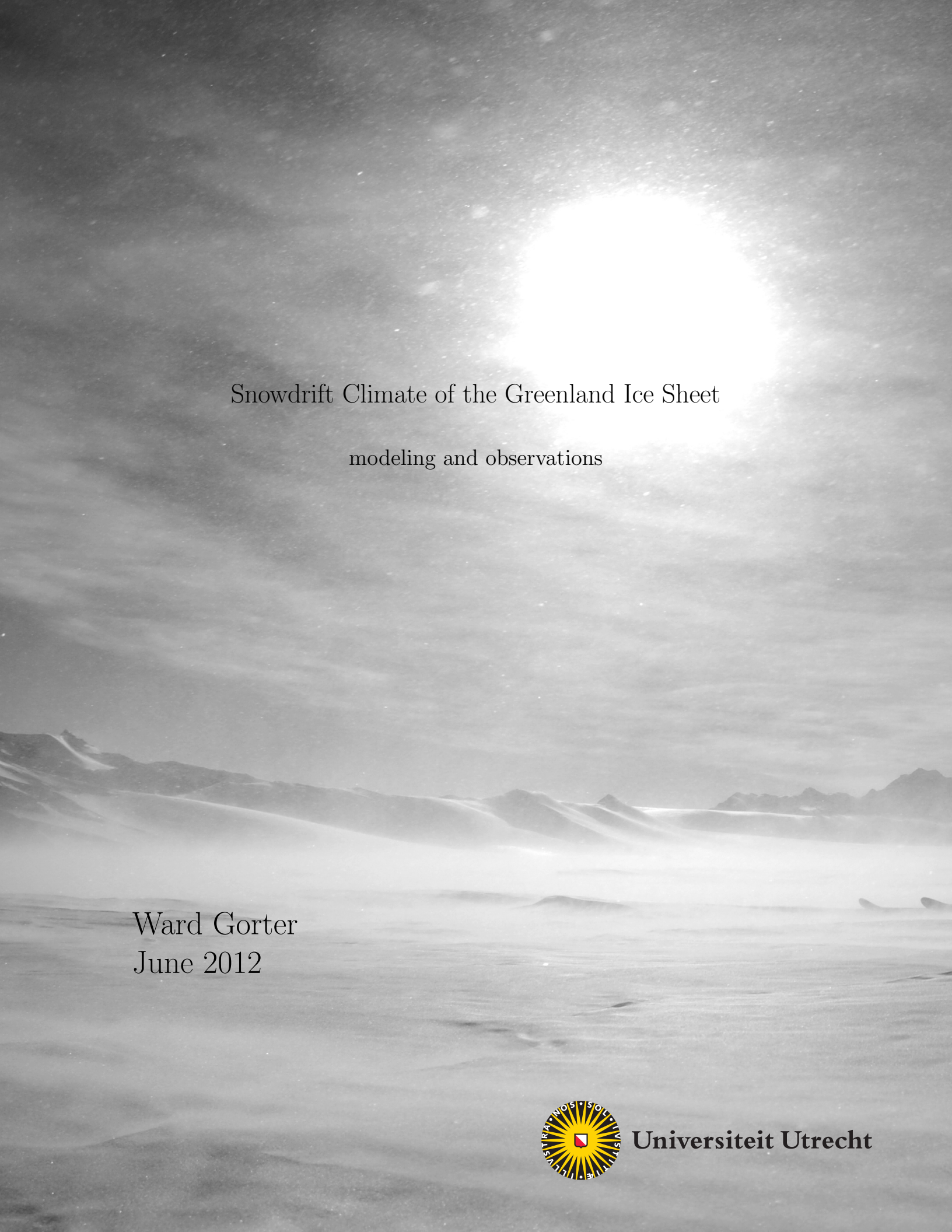

Snowdrift Climate of the Greenland Ice Sheet

modeling and observations

Ward Gorter

June 2012

Universiteit Utrecht

Institute for Marine and Atmospheric research Utrecht (IMAU)
Department of Physics and Astronomy
Faculty of Science
Utrecht University

Cover: Drifting snow near Patriot Hills, Antarctica.

(Taken from:http://weather.thisconnect.com/2010/05/kite-greenland-2010-forecast-may-21-day-17/)

Snowdrift Climate of the Greenland Ice Sheet

modeling and observations

Master's Thesis

by

Ward Gorter
Utrecht University

July 2012

Supervisor:
Prof. dr. M. R. van den Broeke
Institute for Marine and Atmospheric Research Utrecht

Co-supervisor:
J. T. M. Lenaerts, MSc
Institute for Marine and Atmospheric Research Utrecht

Universiteit Utrecht

Abstract

This thesis presents the drifting snow climate of the Greenland ice sheet, from the combined use of Automatic Weather Stations (AWS) from the K-transect and a high-resolution (∼11 km) regional climate model (RACMO2). In the absence of melt, snowdrift sublimation is an important ablation process on the Antarctic ice sheet, where it is relatively well documented. In sharp contrast, no reliable observations of drifting snow exist to date on the Greenland ice sheet. Therefore, the modeled and observed near-surface climate is evaluated instead, showing that RACMO2 is able to realistically simulate temporal and spatial variability of wind speed, humidity and temperature over the ice sheet. Because of its importance to drifting snow events, the wind distribution is fitted to a two-parameter Weibull distribution. This procedure shows narrow katabatically driven wind distributions in confluence regions in the north, and wider more synoptically driven distributions in the south. Trends in these parameters are uncertain.

Snowdrift transport and frequency correlate strongly with near-surface wind speed. Snowdrift sublimation is important in winter, and locally removes more than 25% of annual average snowfall. In summer, surface snow densities are increased due to snowmelt, and snowdrift is strongly suppressed. For the period 1979-1998 and integrated over the ice sheet snowdrift sublimation (27±3 Gt yr^{-1}) is larger than surface sublimation (20±2 Gt yr^{-1}), and removes 3% of annual average snowfall. Runoff (412±87 Gt yr^{-1}) is the dominant ablation factor. Snowdrift erosion is only locally important as a redistributor of snow.

The response of the Greenland ice sheet to a changing climate was investigated by forcing it with the IPCC RCP4.5 scenario, which constitutes a constant radiative forcing of 4.5 Wm^{-2} in 2100. It was found that the resulting temperature increase causes melt to increase from 593±127 Gt yr^{-1} to 1500±217 Gt yr^{-1}, precipitation to increase from 879±119 Gt yr^{-1} to 1007±74 Gt yr^{-1}, while snowdrift sublimation showed no significant change from 26±3 Gt yr^{-1} to 25±2 Gt yr^{-1}. Snowdrift sublimation increases on the plateau and in the north, where increased temperatures favor sublimation, but decreases along the western and southeastern coast, where the limiting effects of melt dominate instead. Changes of the wind distribution are shown to be linked to changes in the temperature deficit layer, but are generally small. Cold air pooling is strongly reduced over the sea ice in the northeast, and moderately so over the tundra around the continent. Changes of the wind distribution are much more subtle than changes of the mass balance. Overall, this thesis shows that the snowdrift climate is intricately linked to the temperature, humidity and wind climate of the Greenland ice sheet. Although much smaller than melt, and certainly less sensitive to climate change, snowdrift processes will remain an important component of the mass budget.

Preface

This thesis is the final product for the fulfillment of the requirements for the degree of master of science at Utrecht University. Over eight months of independent research have led to this report. It has been quite an experience writing this thesis. I found it very motivating to delve into a particular subject and investigate in depth the processes at work. This work would not have been possible without the support of many of my friends, colleagues and family.

First and foremost, I wish to thank Michiel van den Broeke and Jan Lenaerts, who have supported me continuously during the project. As supervisors you have given me countless ideas during our discussions, help whenever needed, and an amazing opportunity to be involved in ongoing scientific work of great relevance. You have motivated me to work on this project with great pleasure, and you have given me an exciting chance to be involved in a fieldwork campaign on the Greenland ice sheet. With these contributions you have helped shape this thesis. I also want to thank Jan van Angelen for providing data on the momentum budget, and his help in interpreting and analyzing it.

Furthermore I wish to thank all those at IMAU that I talked to, listened to, or laughed with over the past year. In particular, I owe thanks to my fellow students in the *student room*. Countless coffee breaks, lunches, talks, drinks and classes we spent together, and I cannot imagine my time here without you. Thank you for the good times, and thank you for the support. Finally I want to thank my family and friends for the interest in the project and their support.

Contents

List of Figures

List of Tables

1 Introduction

Global climate change has instigated intensified research to understand and predict the Earth's climate. Changing global temperatures have significantly altered the climate, although the response is strongly regional. Particularly in the high latitudes the response of the climate system is strong. These changes include a temperature increase well above the global average (Hansen et al., 2010), a strong decline in summer sea ice extent and ice thickness on the Northern hemisphere (Comiso et al., 2008), a decline of most glaciers and icecaps worldwide (Oerlemans, 2005), and a decline in the worlds two large ice sheets: Greenland and Antarctica (Rignot et al., 2011). The Greenland ice sheet contains a volume of ice that is equivalent to 7.3 m of global sea level rise (Bamber et al., 2001), Antarctica nearly ten times more. It is clearly of the utmost importance to monitor and understand their behavior.

The reason why the polar regions are so sensitive to climate change lies in some unique characteristics and feedbacks. The albedo, or shortwave reflectivity, of snow and ice is very high, limiting the amount of absorbed shortwave radiation. The albedo of fresh snow is higher than that of firn, ice or water. When temperatures increase, more melt and snow metamorphism occurs, decreasing the albedo, increasing the amount of absorbed radiation and further increasing melt. This positive feedback, known as the ice-albedo feedback, is particularly important for sea ice. When (summer) sea ice disappears, it is replaced by ocean water, which absorbs much more solar energy. However, this feedback also directly affects the surface mass balance of the Greenland ice sheet and surrounding tundra, where in the ablation zone fresh snow is increasingly replaced by melting snow with a lower albedo, strengthening heat absorption and melt. In the accumulation zone of the ice sheet, this feedback works in the opposite direction, because increased snowfall increases the albedo there (Box et al., 2012).

Ice sheet features such as albedo, accumulation and melt are all strongly influenced by atmospheric conditions. Therefore, extensive observational campaigns were carried out to measure the climate near the Greenland ice sheet. A convenient way to monitor the Greenland climate is by the use of Automatic Weather Stations (AWS). These stand-alone measurement devices continuously monitor near-surface temperature, wind speed, humidity and radiation balance and other variables of interest. Several networks of AWS are noteworthy. Firstly, the Greenland Climate Network (GC-net) that was set up in 1995 comprises a network of 15 AWS covering most climatic regions of the ice sheet (Steffen and Box, 2001). The Danish Meteorological Institute (DMI) has set up a network of AWS in the surroundings of the ice sheet (Cappelen et al., 2001). The Institute for Marine and Atmospheric research Utrecht has a line of three AWS located in the ablation zone in southwest Greeland known as the K-transect since 2003 (Van de Wal et al., 2005). Finally, the Danish Geological Survey of Denmark and Greenland (GEUS) has started a new program called PROMICE in 2007, which consists of 14 AWS in the Greenland ablation zone (Van As et al., 2011). These programs are essential because they form the basis of our understanding of the processes that determine the near-surface climate and energy balance of the Greenland ice sheet. Furthermore, they serve as the ground-truth for the remote sensing techniques and are essential in validating and improving regional climate models. However, spatial coverage remains poor and timeseries only extend roughly 20 years back.

From these measurements a broad picture of the Greenland climate can be formed. Most notably the climate of the Greenland ice sheet is characterized by a quasi-permanent potential temperature deficit and a resulting katabatic circulation (Ettema et al., 2010a). The potential temperature deficit is defined

as the difference between the actual surface potential temperature and that of the free troposphere, extrapolated to the surface (Van den Broeke et al., 1994). Due to a negative radiation balance in winter and surface melt and nighttime cooling in summer, sensible heat is continuously transferred from the air to the surface creating a temperature deficit. The cold and dense air is forced downhill, resulting in a persistent low level katabatic circulation (Heinemann, 1999). Downward atmospheric motion in response to divergence of these katabatic winds creates a shallow high pressure system over the ice sheet. This relatively steady picture is disturbed somewhat by cyclones from the North-Atlantic storm track, that move eastward along the southern tip of the ice sheet. The topography of the ice sheet has a pronounced effect on the flow patterns, and orographic lifting results in large amounts of precipitation along the south-eastern and western coast (Ettema et al., 2009). The ice sheet can further be divided into an accumulation zone where yearly average specific surface mass balance is positive, and a ablation zone where mass is lost. In the cold interior, melt is rare or absent and mass accumulates. In a narrow band close to the edge melt is common and mass is lost.

Both obervations and modeling studies show that the Greenland ice sheet is losing mass and contributing significantly to sea level rise (Rignot et al., 2011, 2008; Van den Broeke et al., 2009). A declining Greenland ice sheet has major consequences on both the regional and global scale, sea level rise being the most prominent example. Eustatic sea level rise is directly influenced by Greenland mass loss, although it must be stressed that local relative sea level rise may vary greatly (Slangen et al., 2012). Furthermore, the polar regions play an important role in the Earth's energy budget. Heat is gained in the tropics, and heat is lost near the poles because of the high surface albedo. Reducing the extent and duration of ice/snow cover reduces this heat loss, which has global consequences. Furthermore, freshwater discharge in the Arctic region influences the global ocean circulation that transports heat from the equator to the poles. This meridional overturning circulation is driven by sinking motion in the Arctic due to increased density of the water as it cools. Freshwater, which has a lower density, may disturb this process and weaken the circulation. This can affect the global oceanic heat transport.

The mass balance of the Greenland ice sheet is the sum of mass fluxes on the ice sheet. Because of the large impact of the Arctic region on the global climate, it is imperative to monitor the mass balance of the Greenland ice sheet. Three large-scale methods to do this have been developed. First, the mass balance can be estimated using repeat altimetry. Measured changes in height can be used to calculate volume changes of the ice sheet. The crucial step is to convert these volume changes to mass changes, using the density. Secondly, mass changes can be measured through changes in the Earth's gravity field. However, gravity changes also come from a wide range of other processes such as tides and crustal movements. Therefore, extensive data filtering is required before a useful signal is derived. The third method is known as the mass balance method, and it requires that all terms (i.e. solid ice discharge across the grounding line, precipitation, meltwater runoff, surface sublimation, and drifting snow sublimation and erosion) in the mass budget are quantified. Because of the sparsity of measurements in the Arctic, this method often relies on the use of regional climate models. For some time, the estimates of the different methods showed considerable difference. Figure 1.1 shows a variety of mass balance estimates and their uncertainty. Clearly, not all estimates lie within the uncertainty range of one another, and a wide variety of estimates is shown. In part this is explained by the fact that mass balance is not constant in time and the estimates span different periods. Nevertheless, a large part of the uncertainty comes from the uncertainties inherent in the different methods. Recently, different methods have shown considerable convergence (Rignot et al., 2011).

Estimates show that in the 1970's and 1980's the Greenland ice sheet was in a near-balance state (Rignot et al., 2008), where accumulation of approximately 700 Gt yr^{-1} was balanced by calving of 480 Gt yr^{-1} and runoff of 220 Gt yr^{-1} (Box et al., 2012). Beginning in the 1990's, an increasingly negative mass balance was found (Rignot et al., 2008, 2011). A mass balance of -166 Gt yr^{-1}, equivalent to 0.46 mm yr^{-1} of global sea level rise, was found for the period 2000-2008 (Van den Broeke et al., 2009). This result was found with a mass budget method, and verified with gravity measurements from the GRACE satellites. Furthermore, an acceleration of -21$\pm$1 Gt yr^{-2} of the mass loss of the Greenland ice sheet was found over the period 1992-2010 using a mass balance approach. Again, the result compared well to the GRACE gravity satellites estimate of -17$\pm$8 Gt/yr^2 from 2003-2010 (Rignot et al., 2011).

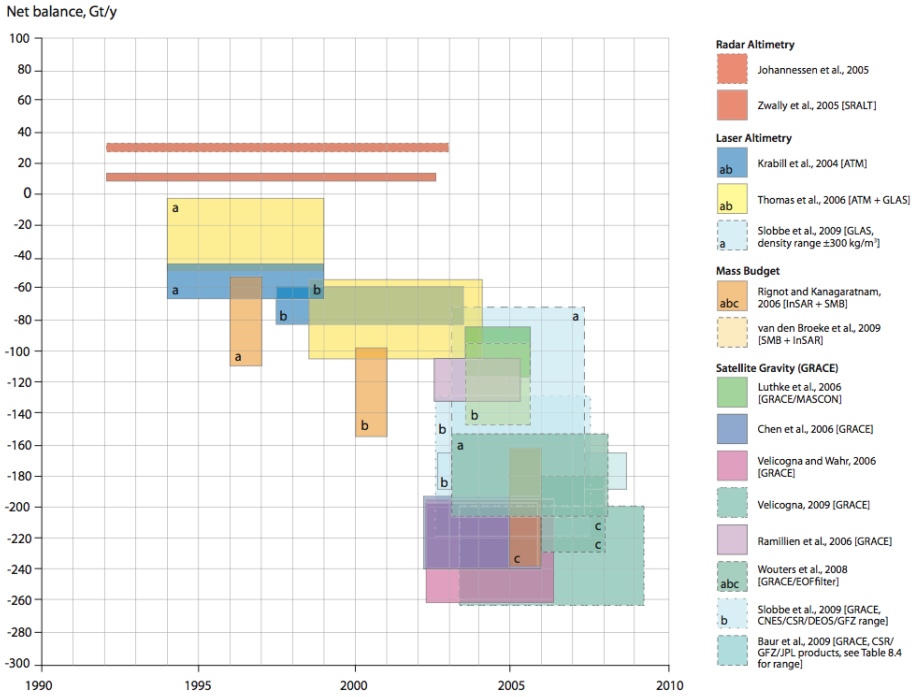

Figure 1.1: Mass balance estimates of the Greenland ice sheet. Different colors represent different methods. The rectangles represent time span over which the measurements apply and the estimated range, given as mean ± uncertainty as given in the original papers. Figure was taken from AMAP (2011)

Finally, Van den Broeke et al. (2009) were able to show that mass loss was about equally split between surface processes and ice sheet dynamics.

The acceleration of mass loss is partly due to increased mass loss by calving. Before 1990, ice discharge rates are estimated by Reeh (1994) and Bigg (1999) as 316 Gt yr^{-1} and 170-270 Gt yr^{-1} respectively (AMAP, 2011). More recently, estimates from Rignot and Kanagaratnam (2006) show accelerating calving rates of 321 Gt yr^{-1} in 1995 to 354 Gt yr^{-1} in 2000 an 421 Gt yr^{-1} in 2005. Between 1995 and 2000 many outlet glaciers south of 66°N accelerated, often even doubling their flow velocity. By 2005, this pattern extended to 70°N. Along with the acceleration and thinning of outlet glaciers, a widespread retreat of the glaciers terminus was observed. Furthermore, this retreat appears to be strongly correlated with air temperatures (Moon and Joughin, 2008). However, Holland et al. (2008) suggest that ocean temperatures may also play a crucial role. The spatial patterns are complex however, and care must be taken when interpreting and generalizing the results. Box and Decker (2011) provide a discussion of some hypothesized causes of these changes and references to the corresponding literature.

The second cause of the increasing mass loss of the Greenland ice sheet is a decreased surface mass balance since the 1990's. (Rignot et al., 2011; Van den Broeke et al., 2009). The atmosphere over the Greenland ice sheet has warmed considerably since the 1990's as a result of global warming (Hanna et al., 2008; Box and Cohen, 2006; Hansen et al., 2010). Figure 1.2 shows the 2005-2011 temperature anomaly of the Arctic and Antarctic region with respect to the period 1970-1990. The sensitivity of the Arctic region is evident. This temperature increase has caused a significant increase of 3% per year in melt and runoff because it increases the ablation area and the duration of the ablation seasons (Ettema et al., 2009). The large increase in melt and runoff is partly counteracted by increased

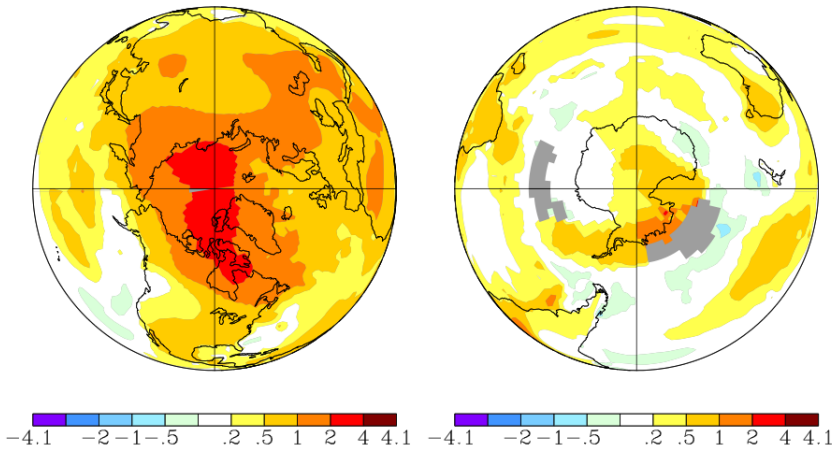

Figure 1.2: 2005-2011 temperature anomalies in °C for the Northern hemisphere (left) and the Southern hemisphere (right) relative to the period 1970-1990. Data and figure are obtained from NASA's Goddard Institute for Space Studies Surface Temperature Analysis (http://data.giss.nasa.gov/gistemp/).

snowfall in the interior of the ice sheet, where temperatures remain below the freezing point. However, raised temperatures also increase the fraction of liquid precipitation and consequently also increase the heat content of the snowpack, further enhancing melt (Ettema et al., 2009; AMAP, 2011). Surface sublimation and evaporation are typically an order of magnitude smaller than runoff, when considering the mass balance of the total ice sheet. Ettema et al. (2009) found a small positive trend in sublimation in recent decades.

Until recently, studies investigating the near-surface climate or mass balance of the Greenland ice sheet have usually neglected processes of drifting snow (Fettweis, 2007; Hanna et al., 2005; Ettema et al., 2009). Snowdrift processes are known to be important in Antarctica where temperatures are so low year-round that melt is of little importance. Therefore, in Antarctica snowdrift sublimation is an important term in the mass budget in regions where the climate is dry and windy. Whereas the snowdrift climate on Antarctica is relatively well studied (Lenaerts and van den Broeke, 2012; Lenaerts et al., 2010; Palm et al., 2011), much less is known about the snowdrift climate of Greenland. Snowdrift sublimation over Greenland was first estimated by Déry and Yau (2002), who provided a first order estimate of the large scale effect of blowing snow. The same snowdrift routine was used by Box et al. (2006) who present the change of snowdrift sublimation in a warming climate. Both studies calculate snowdrift sublimation as a parameterized function of windspeed, but neglect the effect this has on the atmosphere and snow surface. Yet several studies have shown the importance of these feedbacks (Bintanja, 2001; Gallée et al., 2001; Lenaerts et al., 2010, 2012a). Recently, Lenaerts et al. (2012b) presented a study with a high-resolution regional climate model that investigates the spatial and temporal variability of snowdrift sublimation and snowdrift transport using an interactive snowdrift routine. Direct measurements of drifting snow on the Greenland ice sheet are very rare. Several campaigns in the International Geophysical Year (IGY, 1957-1958) were undertaken, but the data is poorly documented.

This thesis is meant to present a broad perspective on the snowdrift climate of the Greenland ice sheet. Snowdrift depends crucially on temperature, humidity and wind characteristics. Using output from the regional climate model RACMO2, spatial and temporal patterns of temperature, humidity and wind speed will be presented. For the first time, a Greenland-wide classification of the wind distribution in terms of the two parameter Weibull distribution is calculated. Model results are compared with independent data from three Automatic Weather Stations. Furthermore, an attempt is made to identify footprints of snowdrift sublimation in AWS data that lack direct measurements of

snowdrift. Model fields of drifting snow are shown to gain a detailed understanding of these events. To investigate the response of blowing snow to changes in the Greenland climate, model runs of 1981-1999 are compared to model runs for 2081-2099. Finally, the momentum budget in the atmospheric boundary layer is solved in an attempt to show explicitly the forcing mechanisms that underly these wind changes.

Chapter 2 develops the theoretical concepts and mathematics that are fundamental to the description of the snowdrift climate. In particular, the forcings in the atmospheric boundary layer and the surface mass budget are specified. Particular attention is given to the description and parameterization of snowdrift. Chapter 3 provides a description of the regional climate model RACMO2, the automatic weather stations that were used in this study and the tool that was used to calculate the momentum budget of the atmospheric boundary layer. Chapter 4 presents the present day climate of the Greenland ice sheet, while Chapter 5 deals with future changes thereof. Chapters 6 and 7 contain the discussion and conclusions.

2 Theory

To facilitate understanding and discussion of the results of this thesis, this chapter is devoted to an introduction of the physical principles that are central to this research. Although far from exhaustive, this introduction is intended to create a thorough understanding of the basic physical principles that can be built upon in later chapters. The focus of this chapter will be on the description of the atmospheric boundary layer, the near-surface climate and its forcing terms and finally the mass balance. This physical description will be complemented with the relevant mathematics where appropriate.

2.1 Momentum Budget of the Atmospheric Boundary Layer

The mass budget of the Greenland ice sheet is strongly influenced by the near surface climate and lower atmosphere, or more specifically the atmospheric boundary layer. The atmospheric boundary layer can be defined as "the layer of air directly above the Earth's surface in which the effects of the surface (friction, heating and cooling) are felt directly on time scales less than a day, and in which significant fluxes of momentum, heat or matter are carried by turbulent motions on a scale of the order of the depth of the boundary layer or less" (Garratt, 1994). The horizontal momentum equations for the boundary layer are the following:

$$\frac{du}{dt} = -\frac{1}{\rho}\frac{\partial p}{\partial x} + fv - \frac{\partial \overline{(u'w')}}{\partial z} \tag{2.1a}$$

$$\frac{dv}{dt} = -\frac{1}{\rho}\frac{\partial p}{\partial y} - fu - \frac{\partial \overline{(v'w')}}{\partial z} \tag{2.1b}$$

Here, the left hand side represents the material derivative, which comprises the local time derivative and the horizontal (ADVH) and vertical (ADVV) advection terms. The first term on the right hand side is the pressure gradient force (PGF), the second is the Coriolis acceleration (COR) and the third represents turbulent friction (FDIV). At present, the PGF includes both large scale effects and boundary layer effects. It is insightful to split it into three components that allow us identify the physical processes that make up the total PGF. To this end, we must first consider the structure of the atmosphere over the Greenland ice sheet.

Above the atmospheric boundary layer, the atmosphere is always stably stratified, meaning that potential temperature increases with height. Conveniently, the potential temperature profile for the free troposphere can be approximated by a linear function (Van den Broeke and Van Lipzig, 2003):

$$\theta_0(z) = \theta_0(0) + \gamma_\theta z \tag{2.2}$$

In the ABL however, a quasi-permanent potential temperature deficit exists over the ice sheet, such that this profile no longer holds.

$$\Delta\theta(z) = \theta(z) - \theta_0(z) \tag{2.3}$$

This temperature deficit is created for two reasons. In winter, negative radiation balance cools the surface over the entire ice sheet, and a compensating sensible heat flux towards the surface cools the

overlying air. This situation persists in summer over the high northerly parts of the ice sheet due to high surface albedo (Ettema et al., 2010a). In summer, the temperature of the ice sheet surface is limited to the melting point, and a small positive or sometimes negative latent heat flux towards the atmosphere exists. This flux is compensated by a positive radiation balance and again a sensible heat flux from the air to the surface (Ettema et al., 2009; Van den Broeke et al., 1994). The result is a temperature deficit that persists year-round. This temperature perturbation allows us to split the pressure gradient force into a large scale component (LSC), a katabatic component (KAT) and a thermal component (THW). Outside the ABL, advection and friction are small, and the dominant balance is between the (large scale) pressure gradient and the Coriolis acceleration.

$$-\left[\frac{1}{\rho}\frac{\partial p}{\partial x}\right]_{LSC} = f v_{LSC} \tag{2.4a}$$

$$-\left[\frac{1}{\rho}\frac{\partial p}{\partial y}\right]_{LSC} = -f u_{LSC} \tag{2.4b}$$

This is known as geostrophic balance, and it implies that the large scale contribution can be written in terms of v_{LSC}. Following Van den Broeke and Van Lipzig (2003) v_{LSC} is assumed to be in thermal wind balance with the background potential temperature profile θ_0, meaning that it changes with height in the presence of a horizontal potential temperature gradient:

$$\frac{\partial u_{LSC}}{\partial lnp} = +\frac{R_d}{f}\left(\frac{p}{p_0}\right)^{\frac{R_d}{c_p}}\frac{\partial \theta_0}{\partial y} \tag{2.5a}$$

$$\frac{\partial v_{LSC}}{\partial lnp} = -\frac{R_d}{f}\left(\frac{p}{p_0}\right)^{\frac{R_d}{c_p}}\frac{\partial \theta_0}{\partial x} \tag{2.5b}$$

These relations are valid outside the ABL, but can be extrapolated to yield the value for v_{LSC} inside the ABL, needed to compute the large scale contribution of the pressure gradient.

The second component KAT results from the negative buoyancy of the cold and dense air of the temperature deficit layer. Over sloping surfaces this air will start to flow downhill. Since the density of the air is inversely proportional to the temperature, the forcing can be shown to increase with increasing temperature deficit. Furthermore, the forcing will be larger over steep slopes. If the downslope direction is defined as the x-direction, this can mathematically be expressed as:

$$-\left[\frac{1}{\rho_0}\frac{\partial p}{\partial x}\right]_{KAT} = -g\frac{\Delta\theta}{\theta_0}sin\alpha \tag{2.6}$$

The meaning of this equation can be understood by assuming a temperature deficit layer (TDL) of constant height, where the top of the TDL follows the ice sheet topography. When comparing two points in the TDL with the same height above sea level, the point closest to the ice sheet interior will be located deeper in the TDL than the one nearest to the ice sheet margin. Therefore, more dense air lies over the point closest to the ice sheet interior, where the pressure is consequently higher. This creates a horizontal pressure gradient directed towards the ice sheet margin, called the katabatic pressure gradient.

The third term THW deals with changes in the height of the TDL. Analogously to the discussion above, the greater the temperature deficit and the TDL height, the higher the pressure difference in the ABL will be. The different pressure increase between two points gives rise to a third pressure term that is known as the thermal pressure gradient force. This term can therefore be written as:

$$-\left[\frac{1}{\rho_0}\frac{\partial p}{\partial x}\right]_{THW} = \frac{g}{\theta_0}\frac{\partial \hat{\theta}}{\partial x} \tag{2.7}$$

where $\hat{\theta}$ is the integrated temperature deficit:

$$\hat{\theta}(z) = \int_{z}^{h_s+h} \Delta_\theta(z')dz'. \tag{2.8}$$

where the upper integration limit is chosen well above the top of the TDL. The advantage of this method is that no precise definition of the top of the TDL is required. It should be noted that these definitions of KAT and THW can lead to strong forces of opposite direction over steep topography. Here commonly the top of the TDL is approximately flat, such that THW is directed upslope, while KAT is directed downslope. If the top of the TDL is exactly flat, the two forces are of equal magnitude (Van den Broeke and Van Lipzig, 2003). The resulting full equations of motion, where the x-direction is defined downslope, are then the following:

$$x-mom: \quad \frac{\partial u}{\partial t} = -u\frac{\partial u}{\partial x} - v\frac{\partial u}{\partial y} - w\frac{\partial u}{\partial z} + \frac{g}{\theta_0}\frac{\partial \hat{\theta}}{\partial x} + fv - fv_{LSC} - \frac{\partial \overline{(u'w')}}{\partial z} + \frac{g}{\theta_0}\Delta_\theta sin\alpha, \tag{2.9a}$$

$$y-mom: \quad \frac{\partial v}{\partial t} = -u\frac{\partial v}{\partial x} - v\frac{\partial v}{\partial y} - w\frac{\partial v}{\partial z} + \frac{g}{\theta_0}\frac{\partial \hat{\theta}}{\partial y} - fu + fu_{LSC} - \frac{\partial \overline{(v'w')}}{\partial z}. \tag{2.9b}$$

In these equations the three contributions to the PGF are conveniently separated. For modeling purposes, this separation is not required, and the original equations are solved for simplicity. To investigate the forcing terms of the atmospheric boundary layer an analysis of the momentum budget is performed diagnostically and offline that exploits the separation of the pressure gradient force. This is further explained in Section 3.3. Section 2.2 will present the different terms in the mass balance and Section 2.3 will discuss the turbulent structure of the surface layer and the physics of drifting snow.

2.2 Surface Mass Balance

The mass balance (MB) of an ice sheet is made up of two major components, the surface mass balance (SMB) and the solid ice discharge (D):

$$MB = SMB - D \tag{2.10}$$

Typically the SMB integrated over the ice sheet is positive, and this mass gain is compensated by a mass loss through solid ice discharge. For an ice sheet in balance these terms exactly cancel. Solid ice discharge was discussed briefly in the introduction and will not be discussed further. The surface mass balance represents the sum of all processes that add or remove mass from the surface. Integrated over a year, the ice sheet typically consists of an area of positive specific surface mass balance (SSMB) in the interior, called the accumulation zone, and of negative SSMB near the edges, called the ablation zone. The line where the SSMB is zero is called the equilibrium line. The SMB is dominated by snowfall and runoff. Snowfall represents roughly 92% of accumulation, while runoff constitutes 90% of ablation (Ettema et al., 2009). The position of the equilibrium line strongly depends on height due to the atmospheric lapse rate of temperature. In the lower and warmer regions of the ice sheet melt dominates, while in the higher cold regions the occurrence of melt is severely limited and exceeded by snowfall. The steep ice sheet slopes near the coast limit the extent of the ablation zone, such that it only covers 10% of the ice sheet surface (Ettema et al., 2009). Since SMB is dominated by snowfall and runoff, a first approximation of its sensitivity to climate change can be attained by looking at changes of these two variables. Oerlemans et al. (2005) found a climate sensitivity of 49 mm K^{-1} for runoff and 3.8 mm $\%^{-1}$ for precipitation. Furthermore, Gregory and Huybrechts (2006) found a climate sensitivity of 5% K^{-1} for precipitation. Combined, these yield a sensitivity of 19 mm K^{-1} for precipitation versus 49 mm K^{-1} for runoff (AMAP, 2011). This result shows that both melt and precipitation increase in a warming climate, with melt changing significantly faster. This is consistent with observations over the past decades.

However, to gain a more complete understanding of the SMB the first order approach taken above is not sufficient and all components must be considered in detail. The SMB can be written mathematically as:

$$SMB = \int_{year} (P - SU_s - RU - \nabla \cdot TR_{ds} - SU_{ds})dt \tag{2.11}$$

It is composed of precipitation (P), surface sublimation (SU_s), runoff (RU), snowdrift erosion ($\nabla \cdot TR_{ds}$) and snowdrift sublimation (SU_{ds}). Precipitation includes both solid precipitation in the form of hail and snow and liquid precipitation. Surface sublimation may also be negative, implying surface deposition. Runoff is meltwater that does not refreeze but flows to the surrounding oceans. Snowdrift erosion is the local horizontal divergence of the flux of blowing snow, and may contribute both positively and negatively to the SMB. Snowdrift sublimation represents sublimating particles of snow that have been lifted in the air. Its contribution to the SMB is always negative.

Precipitation is mainly controlled by the water vapor holding capacity of the atmosphere. Air can hold a maximum amount of water vapor, known as the saturation vapor pressure. The saturation vapor pressure depends strongly on temperature through the Clausius-Clapeyron relation. Qualitatively, this relation states that warm air can hold more moisture. Precipitation therefore typically occurs when rising air cools adiabatically, lowering the saturation vapor pressure until condensation occurs. In Greenland this rising motion is often due to orographic lifting, resulting in high values of precipitation along the coast. In the interior, little precipitation falls due to the extremely low air temperatures and atmospheric moisture content.

Surface sublimation occurs only when the surface is below the freezing point and the air is subsaturated with respect to ice. When surface temperatures are at the melting point, melt and evaporation will dominate rather than sublimation. Deposition (i.e. negative surface sublimation) also occurs when temperatures are below the freezing point, but the air needs to be supersaturated with respect to ice. The surface then acts as a medium on which condensation can occur. Supersaturation typically occurs at extremely low temperatures.

The physical processes that cause melt are well understood. When the surface energy balance (SEB) is positive, the surface layer will heat up. When the temperature reaches the melting point, melt will occur. Modelling the SEB is an appealing approach, but not all terms are well constrained. Observational studies lack spatial coverage. Therefore, modelling estimates of melt differ strongly (Hanna et al., 2005; Fettweis, 2007; Ettema et al., 2009; Box and Cohen, 2006). Furthermore, meltwater can be kept in place through capillary retention or refreezing, further complicating estimates of runoff. Nevertheless, different methods generally agree on the trends of melt and runoff (AMAP, 2011).

The last two components of the SMB are the main topic of this thesis and will be considered in the following section.

2.3 Physics of Drifting Snow

Blowing snow is an example of two-phase flow, where solid snow particles are suspended in air. This state can be maintained when the upward fluid drag exceeds the downward gravitational pull on the particles (Bintanja, 2000a). For snowdrift to occur, the shear stress exerted by the wind on the snow surface must be large enough to break cohesive bonds between particles at the surface. To maintain suspension, turbulent kinetic energy is required. Clearly, the wind profile and turbulent structures are critical for the onset and maintenance of snowdrift. Therefore, the structure of the surface layer winds will be discussed briefly below.

Over the Greenland ice sheet the boundary layer is mostly stably stratified, although strong winds may induce near-neutral stratification. To investigate the wind characteristics in this case, the wind is often conveniently split up in an average part and a turbulent fluctuation. The time average of these fluctuations is zero by definition. This procedure is known as Reynolds decomposition. Details of this procedure for the neutral ABL can be found in for example Garratt (1994) or any other standard textbook on boundary layer meteorology. Further using the well known Bousinesq approximation,

horizontal homogeneity and incompressibility yields the following equation of motion:

$$\frac{du}{dt} = -\frac{1}{\rho}\frac{\partial p}{\partial x} + fv - \frac{\partial \overline{(u'w')}}{\partial z}. \tag{2.12}$$

The left hand side comprises the local derivative and advection terms as given in Equation 2.9a. The first term on the right represents the combined effect of KAT, LSC and THW, while fv still represents the coriolis acceleration. The last term represents friction. Since the variables u' and w' are not explicitly defined, this equations cannot straightforwardly be solved. This is known as the closure problem. A common approach to solve this is to express this term as a gradient of the time-averaged counterpart of the fluctuation and a constant of proportionality. One such approach is known as mixing length theory:

$$\overline{(u'w')} = -l^2 \left(\frac{\partial u}{\partial z}\right)\left|\frac{\partial u}{\partial z}\right|, \tag{2.13a}$$

$$\overline{(v'w')} = -l^2 \left(\frac{\partial v}{\partial z}\right)\left|\frac{\partial v}{\partial z}\right|. \tag{2.13b}$$

where l is the mixing length. These are the turbulent contributions in the horizontal momentum budget. Combined, and taken at the surface they represent a measure of turbulence that is known as the friction velocity u_*:

$$u_*^2 = \left[\overline{(u'w')}^2 + \overline{(v'w')}^2\right]_S^{\frac{1}{2}} \tag{2.14}$$

Adding the squares of Equations 2.13a and 2.13b and taking the square root, we obtain:

$$\left[\overline{(u'w')}^2 + \overline{(v'w')}^2\right]_{SL}^{\frac{1}{2}} = l^2 \left(\frac{\partial V}{\partial z}\right)^2 \tag{2.15}$$

which is valid in the surface layer and where V is the total velocity. Since fluxes in the surface layer are nearly constant with height, it is a good approximation to equate 2.14 and 2.15. Furthermore, near the surface the mixing length l, can be rewritten as κz, where κ is Von Karman's constant. This last result signifies that the effectiveness of mixing is suppressed near the surface because the size of eddies is limited by the presence of the surface. The resulting expression for the friction velocity is then:

$$u_* = \kappa z \frac{\partial V}{\partial z} \tag{2.16}$$

Since the friction velocity is a measure of turbulence, it is not surprising that it is an important quantity that determines the onset of snowdrift events. Many studies have shown that a threshold friction velocity can be defined that controls the onset of snowdrift (Schmidt, 1986; Mann et al., 2000; Doorschot et al., 2004). Typically, threshold values around 0.3 m s^{-1} are reported. However, these reports do not take the characteristics of the snow surface into account. The structure of the snowpack is strongly determined by the shape, size and density of the snowpack (Gallée et al., 2001), all of which change in response to snow metamorphism. Shape and size of the snow particles can be used to define a mobility index. The mobility index is a parameterized measure of the cohesiveness of the snowpack, and so describes whether particles at the surface are prone to uplift by atmospheric turbulence. However, the mobility index is a measure of shape and size of individual snow crystals. The organization of these crystals in the snowpack can roughly be characterized by the density of the upper layers. Fresh snow crystals form a non-cohesive snowpack due to their shape, while large round snow crystals that form in wet conditions form very heavy and cohesive snowpacks (Gallée et al., 2001). Note that although these processes are qualitatively well understood, their quantitative description is based on parameterizations that were obtained from measurements. Because these parameterizations are intended to represent these local measurements, they may not be adequate or appropriate at locations

where different conditions exist. The scarcity of measurements, particularly on the Greenland ice sheet, and the resulting uncertainties must be kept in mind.

Once initiated, drifting snow has several important effects on the atmosphere. Firstly, snow particles have a mechanical effect on the flow. The vertical distribution of snow particles creates negative buoyancy, or increased stability, which results in the destruction of turbulent kinetic energy (TKE), limiting the atmospheric ability to transport snow. Density increases due to snow particles further influence the flow. A detailed discussion can be found in Bintanja (2000b). Secondly, drifting snow particles influence the heat and moisture budget of the flow. Snow particles in undersaturated air show rapid sublimation because they are well ventilated. Moreover, the surface area of snow particles that is exposed to the air rapidly increases when snow is suspended in the air. Therefore, large amounts of snow can sublimate in a short period of time. The heat required for sublimation is extracted from the atmosphere, which cools as a result. Due to moistening and cooling of the air, the relative humidity quickly increases to saturation. Since sublimation is proportional to undersaturation and temperature, the process is self-limiting. Analogously, surface sublimation is strongly limited due to rapid saturation of the air near the surface. A modeling study by Lenaerts et al. (2012b) found that Greenland surface sublimation was 40% lower when snowdrift sublimation was included in the model, while total sublimation increased.

3 Methods

Three data sources were used in this research. Firstly, data from the regional climate model RACMO2 were used to evaluate the near-surface climate and SMB components. Secondly, AWS data were used to evaluate the RACMO2 data and to look for signatures of drifting snow. Finally, the momentum budget was solved explicitly to gain a better understanding of the processes that drive changes in the Greenland wind and drifting snow climate. This chapter will discuss these data sources.

3.1 AWS-Data

The observational data used in this study come from three AWS in the ablation zone of southwest Greenland. The AWS from the Institute for Marine and Atmospheric research Utrecht (IMAU) are part of the so called K-transect near Kangerlussuaq that was set up in 1990 as part of the Greenland Ice Margin Experiment (GIMEX). This transect consists of a line of mass balance measurements along the 67°N latitude, ranging from the ice edge to 1800 m up the ice sheet (Oerlemans and Vugts, 1993; Van de Wal et al., 2005). In August 2003, three AWS were added to the K-transect at three locations that are known as S5, S6 and S9. These are located at 6, 38 and 88 km from the ice edge at 490, 1020 and 1520 m above sea level respectively (Van den Broeke et al., 2008b). Figure 3.1 shows the location of the AWS sites and photos of the local conditions near the AWS. Three regions are distinguishable on the ice sheet. The bare ice zone extends up to roughly 1500 m (greyish), the superimposed ice zone from 1500-1750 m (milky blue) and the percolation zone above that (white). The dry snow zone lies higher on the ice sheet and is not visible in this image (Van den Broeke et al., 2008a). The surroundings of the AWS at the end of the ablation season are indicative for the large gradients in the ablation zone. At S5, the ice surface is very rough and inhomogeneous. Two types of obstacles are found, hummocks of 5-10 m wide and 0.5-2 m high, and domes of 60-120 m wide and 3-4 m high (Smeets and van den Broeke, 2008). At S6 the surface is much smoother, covered with smaller hummocks and intersected by gullies that transport meltwater in summer. In winter these gullies are filled with snow. At S9 the surface is flat and very smooth throughout the year. The surface at S9 may be covered with snow, wet snow or meltwater (Smeets and van den Broeke, 2008). The AWS are mounted on four legs that make a small angle with the horizontal and stand on the surface, so that they are allowed to sink with the lowering surface during the ablation season (Van den Broeke et al., 2008b). The AWS are equipped with sensors for temperature, specific humidity, wind speed, wind direction, pressure, and sensors that measure the radiation budget. The radiative fluxes are measured at 6m height, wind speed and direction, temperature and humidity at both 6 m and 2 m height, while pressure is measured in the electronics box (Van den Broeke et al., 2008b). Van den Broeke et al. (2008a) present an overview of all the individual sensors, their accuracy and mean values of measured variables. Most variables are stored as 30 minute averages, although sampling rates are higher. All data were quality checked before use (Van den Broeke et al., 2008b).

The Kangerlussuaq region, where the K-transect is located, is characterized by a wide strip of hilly tundra more than 100 km wide, intersected by the Kangerlussuaq fjord. Because of this, the climate is dry and very stable (Smeets and van den Broeke, 2008). Average temperatures at the ice edge are $-18°C$ in winter, while in summer they rise to $+9.3°C$ due to heating of the air over the adjacent ice

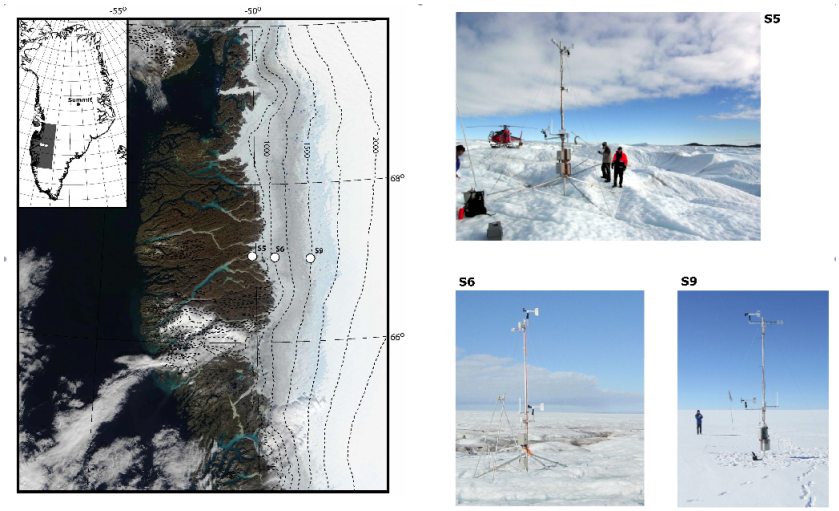

Figure 3.1: Photo of AWS region and local surface conditions at S5(67°06'N,50°07'W), S6(67°05'N,49°23'W) and S9(67°05'N,48°14'W). Taken from Van den Broeke et al. (2008b)

free tundra (Box, 2002). Maximum daily temperature can reach much higher values.

3.2 Model Description

The Regional Atmospheric Climate Model version 2 (RACMO2 hereafter), was developed by Van Meijgaard et al. (2008) and consists of the semi-Lagrangian dynamics kernel of the numerical weather prediction model HIRLAM (Undén et al., 2002), complemented with the physics package of the European Centre for Medium-Range Weather Forecasts Cy23r4 (White, 2001). At the lateral boundaries, the model is forced with ECMWF reanalysis ERA-40 for 1960-1988 and ERA interim for 1989-2011 at 6 hourly resolution (Lenaerts et al., 2012b). The reanalysis fields are calculated with the same physical scheme as RACMO2. Sea ice and sea surface temperature are prescribed from these reanalyses. In the interior domain the model is allowed to evolve freely. The model includes a multi-layer snow scheme, that includes the effects of meltwater percolation, retention and refreezing (Bougamont et al., 2005; Ettema et al., 2010b). Furthermore, it improves the treatment of the interaction between the ice sheet surface and the overlying atmosphere (Ettema et al., 2010b). A new snow albedo has also been included in the model, which treats the effects of snow metamorphism (Kuipers Munneke et al., 2011). The model has 40 hybrid vertical layers, of which the lowest is located roughly 10 m above the ground. This type of vertical coordinate follows topography near the surface, and pressure levels in the free troposphere (Ettema et al., 2010b). The horizontal resolution is 0.1°, or 11 km, sufficient to accurately resolve most of the ice sheet ablation zone and steep climate gradients, except in some regions where the width of the ablation zone is less than the horizontal resolution of the model (Ettema et al., 2010b). To calculate standard meteorological variables at 2 m reference height, similarity theory is used as a way to interpolate to the surface. To this end, assumptions on the roughness lengths of momentum, heat and humidity were made (Ettema et al., 2010b). Finally, a drifting snow routine was added to the model. The threshold friction velocity that determines if the snowdrift routine is initiated is defined as in Gallée et al. (2001):

$$u_{*,t} = u_{*,t_0} exp\left(\frac{-n}{1-n} + \frac{n_0}{1-n_0}\right) \tag{3.1}$$

Here n is the snow porosity:

$$n = 1 - \frac{\rho_s}{\rho_i} \tag{3.2}$$

and analogously n_0 is given as:

$$n_0 = 1 - \frac{\rho_0}{\rho_i} \tag{3.3}$$

where ρ_s is the snow density, ρ_i is the density of ice and ρ_0 is the density of fresh snow, here taken as 300 kg m^{-3}. In the above formulation u_{*,t_0} is defined as:

$$u_{*,t_0} = \frac{log(2.868) - log(1 + Mo)}{0.085} C_D^0.5 \tag{3.4}$$

where Mo is the mobility index, given by:

$$Mo = 0.75DE - 0.5SP + 0.5 \tag{3.5}$$

and C_D is the drag coefficient for momentum given by:

$$C_D = \frac{u_*^2}{u^2} \left(= \frac{\kappa^2}{ln\left(\frac{z}{z_0}\right)} \right) \tag{3.6}$$

This procedure was used by Lenaerts et al. (2012a) over the Antarctic ice sheet. Because no good coverage of reliable measurements of snow structure exist, dendricity (DE) and sphericity (SP) were assumed constant at a value of 0.5. Furthermore, neutral atmospheric conditions are assumed, such that the wind profile can be approximated by a logarithmic function that depends on the aerodynamic roughness length for momentum z_0, which is prescribed. This assumption is quite reasonable during snowdrift conditions, since the strong winds will cause turbulent mixing of the surface layer, reducing the surface temperature deficit and creating neutral conditions. Then, given solely the actual surface snow density, the threshold friction velocity can be determined. This allows us to determine wether snowdrift occurs, and a snowdrift frequency can be determined.

However, problems arise using this approach, because ρ_s is poorly constrained, and few measurements exist. Due to the large sensitivity of snowdrift frequency to surface density this can lead to large errors. Therefore, a parameterization was developed for the surface density in Antarctica, such that modeled snowdrift frequencies agree well with observations. The so obtained surface density is not necessarily realistic, but it ensures that snowdrift frequencies are well represented (Lenaerts et al., 2012a). A multiple linear regression was performed on these densities, such that the density of fresh snow during accumulation events can be expressed in terms of the near surface temperature and wind speed.

This regression was implemented in the present study over the Greenland ice sheet to calculate the surface snow density from available fields of temperature and wind during accumulation events. Applying the same tuning method to the Greenland ice sheet is not viable due to a lack of observations, and so the regression derived for Antarctica is the optimal choice at present.

Once the snowdrift threshold friction velocity is exceeded, the snowdrift routine is activated. Simple parameterizations exist to calculate TR_{ds}, but computations of SU_{ds} are computationally very expensive due to the wide range of particle sizes involved. Here a bulk model for both variables is used for computational efficiency (Lenaerts et al., 2012a). The PIEKTUK model was developed by Déry and Yau (1999) and was shown to compare well with observations (Yang and Yau, 2008) and with other spectral snowdrift models (Xiao et al., 2000). The snowdrift routine uses temperature, specific humidity, pressure to calculate SU_{ds}. During a snowdrift event SU_s is assumed to be zero in response to quick saturation of the surface layer. The latent heat flux thus obtained is extracted from the surface, which cools. A compensating sensible heat flux is then set up that cools the atmosphere. The turbulent diffusion scheme causes the propagation of these signals to higher layers. This method,

where all latent heat release due to sublimation is released at the surface is not physically accurate. However, turbulent mixing is strong in the high-wind conditions of snowdrift events such that the effects quickly propagate upwards.

The model (without snowdrift routine) was thoroughly evaluated against observational data by Ettema et al. (2010b). The overall ability of the model to reproduce the climate is good, although some biases exist. Important for the present purposes is that the model underestimates the frequency of extreme wind speeds, which are important for drifting snow. Unfortunately, no reliable measurements of drifting snow exist on the Greenland ice sheet. Satellite measurements of the drifting snow layer height are limited due to the presence of clouds and shallow drift layers (Lenaerts et al., 2012b).

3.3 Momentum Budget Tool

The determination of the different terms in the momentum budget is based on the division of terms as laid out in the Section 2.1. The numerical model was used by Van Angelen et al. (2011) to describe the recent momentum balance over Greenland. Here, an adapted version of this model will be used that neglects advection terms for simplicity. On the scales and periods we are interested in, this term is known to be small. Only near rough topography these terms will locally be important. The model does account for the active forces LSC, KAT and THW and for the passive forces COR and FDIV. Here, different from Equation 2.3, the background potential temperature θ_0 is linearly extrapolated to the surface as a function of pressure, not height. The sensitivity of the results to the chosen method was investigated by Van Angelen et al. (2011), who found qualitatively the same results. Friction in the model is parameterized, and also separately calculated as a residual from the other terms. The results of both methods are nearly indistinguishable. The vertically integrated potential temperature deficit was obtained by multiplying the height of a layer with the average of the potential temperature of the level above and below and summing over all layers.

4 Present Day Climate of the Greenland Ice Sheet

The climate of the Greenland ice sheet of the last few decades will be presented in this chapter. Aiming to describe the snowdrift climate we must first discuss in detail the wind climate in Section 4.1, the temperature and humidity climate in Section 4.2, before we can turn to a description of snowdrift variables in Section 4.3. Where Chapter 2 discussed the theoretical background of the momentum and mass budget, here the focus will be on temporal and spatial patterns of the climate in the period 1957-2011.

4.1 Wind Climate

The Greenland wind climate is characterized by particularly consistent wind direction and wind speed. Driven primarily by the katabatic forcing, the resulting downslope winds are deflected to the right by the Coriolis acceleration and slowed down by surface friction. In the absence of friction, a balance between the katabatic and Coriolis force would result in flow along the height contours of the ice sheet, but friction maintains a downslope component. Due to the year-round persistence of the katabatic forcing, and the passive nature of FDIV and COR, the wind direction is relatively constant. Figure 4.1a presents the frequency distribution of wind direction as measured by all three AWS. A dominant wind direction can clearly be identified for all three AWS, and this direction is always deflected to the right relative to the downslope direction. The reason for the larger spread of the wind direction at S9 is likely related to the smaller katabatic forcing as a result of a smaller surface slope, and associated increased relative importance of the synoptic forcing. As a data quality check, these frequency distributions were tested for yearly drift of dominant wind direction, but none was found. To quantify the spread of wind direction, the directional constancy is defined as the ratio of the vector average wind speed over the scalar average wind speed (Van den Broeke and Van Lipzig, 2003):

$$dc = \frac{\left(\overline{u}^2 + \overline{v}^2\right)^{\frac{1}{2}}}{\overline{(u^2 + v^2)^{\frac{1}{2}}}} \tag{4.1}$$

A directional constancy of 0 indicates that wind direction is randomly distributed, a directional constancy of 1 indicates winds of constant direction only. For the AWS the calculated directional constancy is 0.90, 0.93 and 0.87 for S5, S6 and S9 respectively. The higher directional constancy at S6 relative to S5 may have to do with surface roughness and topography. These very high values of directional constancy are typical for the large ice sheets (Van den Broeke and Van Lipzig, 2003).

Table 4.1 shows a summary of the mean values of observed and modeled wind speeds and their standard deviations. The model is well able to reproduce the mean state and variability, since the model bias is much smaller than the variability. This result is consistent with the findings of Ettema et al. (2010b) who evaluated the surface wind field of RACMO2 against a larger set of AWS, and similarly found biases much smaller than the variability for all seasons. The frequency distribution

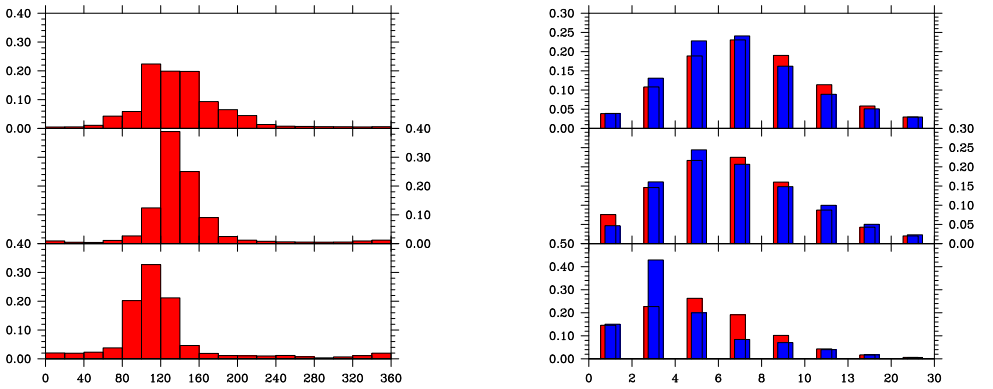

(a) Wind direction (°) frequency distribution

(b) Wind speed (m s^{-1}) frequency distribution

Figure 4.1: Annual frequency distribution (-) of wind direction (°) and windspeed (ms^{-1}) of all three AWS. From top to bottom S9, S6 and S5 are shown. For windspeed, both observations (red) and RACMO2 results (blue) are shown. A linear interpolation was used to convert RACMO2 data to the desired location. Hourly data for the AWS, and three hourly data for RACMO2 were used.

of wind speeds as recorded by the AWS and as modeled by RACMO2 is shown in Figure 4.1b. In accordance with the above results, the model performs well and is able to realistically simulate the wind speed distribution. The most notable difference is an underestimation of the frequency of high wind speeds at S9 and S5, and a corresponding overestimation of low wind speeds, particularly at S5. The relatively poor performance at S5 is likely explained by the insufficient spatial resolution to resolve the outlet of Russell glacier, where it is located (Van Angelen et al., 2012; Ettema et al., 2010b). Despite larger katabatic forcing near the ice margin, a clear decrease in wind velocity is observed from S9 to S5, owing to the increased aerodynamic roughness towards the edge. This translates into an aerodynamic roughness length z_0 that was found to differ by a factor 1000 over the ablation zone at the end of the ablation season (Smeets and van den Broeke, 2008).

	S5 (m s^{-1})	S6 (m s^{-1})	S9 (m s^{-1})
observed 10 m wind	5.3	6.9	7.9
observed σ 10 m wind	3.1	3.9	4.0
modeled 10 m wind	4.5	7.0	7.4
modeled σ 10 m wind	2.9	3.6	3.8

Table 4.1: Annual mean wind speeds and standard deviations from measurements and from RACMO2 at the AWS locations.

The wind speed and direction over the entire Greenland ice sheet and its surroundings is visualized in Figure 4.2. Notable contrasts exist between winds over the ice sheet and winds over the surrounding tundra, the former being much stronger. Lowest annual mean wind speeds (± 2 m s^{-1}) are found over regions where the strip of tundra is wide, particularly in the southwest, north and east. Highest annual mean wind speeds (± 10 m s^{-1}) are found in Dronning Louise Land in the northeast, due to a large surface slope and a very strong temperature inversion. Unfortunately no measurements are available in this region (Ettema et al., 2010a). Over the western part of the ice sheet, a southerly katabatic flow is enhanced by the large scale forcing resulting in relatively strong winds (Van Angelen et al., 2011). The deceleration of the wind towards the ice sheet margin is on the one hand by increasing surface roughness, but also by thermal forcing of the near surface wind. Over the ice sheet, katabatic

winds drain due the sloping surface, but over the flat tundra this forcing diminishes and a pool of cold air builds up (Van den Broeke et al., 1994). This increases the height of the temperature deficit layer such that a thermal forcing works up the ice sheet, opposing the katabatic forcing. Also, in the absence of strong winds and associated mixing, extremely cold and stable conditions develop over the tundra, further limiting strong winds (Ettema et al., 2010a). Over the ocean along both the western and eastern coast of the ice sheet, persistent thermally induced northerly flows are present in winter (Van Angelen et al., 2011).

Average wind speeds are significantly higher in winter (DJF, Fig. 4.2 (middle)) than in summer (JJA, Fig. 4.2 (right)). This can be explained by the stronger katabatic forcing due to low winter cloud cover, enhanced radiative cooling, a stronger polar vortex in winter and lower surface roughness (Ettema et al., 2010a). In all seasons, an anti-cyclonic circulation is present over the ice sheet. Again this is caused by a dominant balance between KAT, COR and FDIV, and LSC in summer.

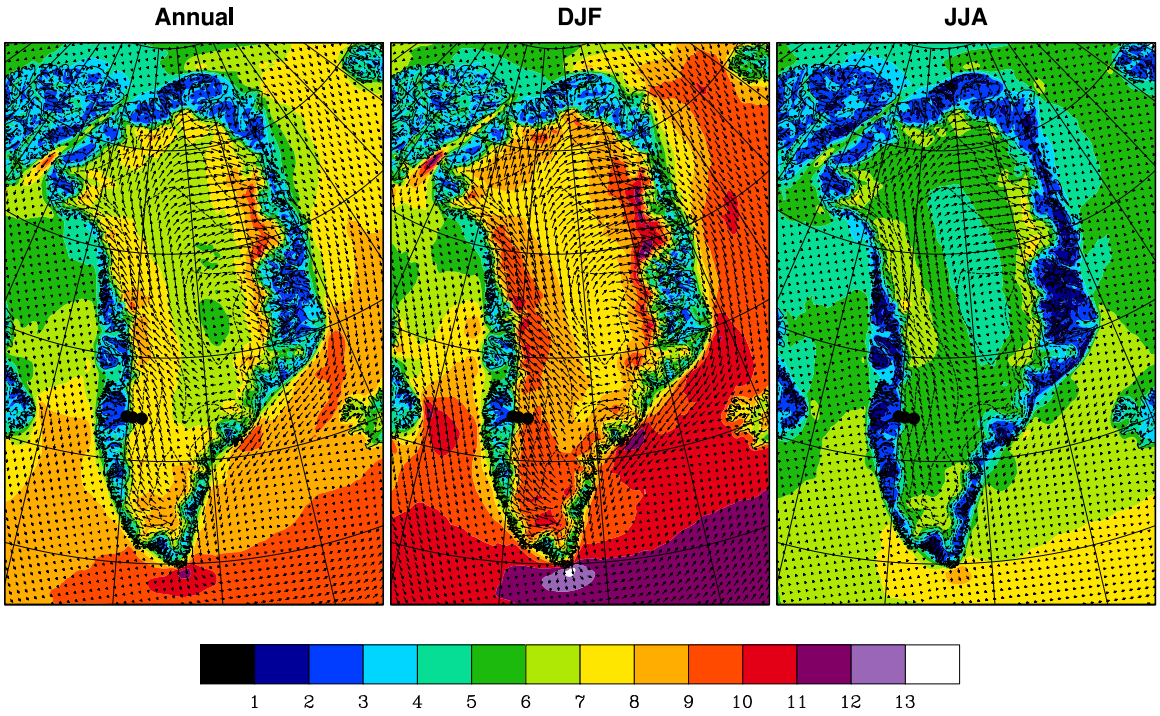

Figure 4.2: 10 m wind speed (m s^{-1}) and direction (°) for annual average, winter and summer. Wind direction vectors represent the vector average velocity of the wind and are plotted every fourth grid point for clarity. The AWS are indicated as black dots.

Figure 4.3 shows annual average values for directional constancy of Greenland and its surroundings. Directional constancy is low over the oceans, where winds are primarily driven by passing synoptic weather patterns and winds are consequently variable in direction. Over land, directional constancy is markedly higher, owing to the presence of persistent downslope katabatic forcing. The low directional constancy over the ice ridge running from the south to the northeast can be explained by the absence of a significant surface slope in that region. In the absence of the katabatic forcing, the wind is again dominated by synoptic patterns and more variable. Figure 4.4 shows the region where the AWS are located and illustrates the complex geographical patterns of wind speed. The AWS, indicated as black dots, clearly lie in different regimes of the wind climate. In the figure, wind vectors are plotted every other gridpoint, which is easily sufficient to resolve the topography and spatial variation of the wind in the region around S9 and above. However, near S5 and over the tundra, small scale topographic features

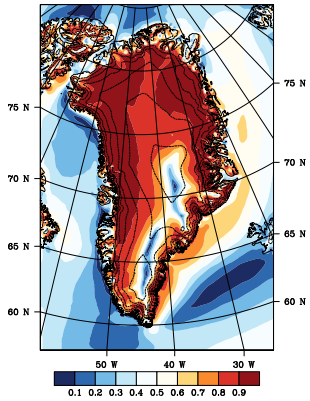

Figure 4.3: Directional constancy (-) of the 10 m daily average wind for 2004-2009

can not always be resolved and the wind pattern that is shown is too homogeneous. Nevertheless, the horizontal resolution of 11 km is easily sufficient to capture most of the spatial variation, especially in the higher regions of the ice sheet where snowdrift is more common.

To assess the temporal performance of the model, Figure 4.5 shows a comparison of observed and modeled daily average wind speed at S9. The model represents the seasonal cycle well, with higher wind speeds in winter and lower wind speeds in summer. Also the increase in wind speed variation from summer to winter is properly represented, suggesting that RACMO2 is able to realistically model the different forcing mechanisms. Wind speed variation on the timescale of days is also very well captured. RACMO2 is even able to capture short-lasting strong wind events (e.g. end of March, early May), although it misses some events (e.g. halfway January). The ability of RACMO2 to model the near surface wind climate, and particularly high wind speed events, serves as a first indication that RACMO2 can similarly produce a realistic snowdrift climate. Remaining biases may have to do with the poorly known spatial and temporal patterns of roughness length and poorly defined stability corrections during very stable conditions that regularly occur (Ettema et al., 2010b).

The preceding discussion has characterized the wind climate by its spatial patterns and temporal variability. The frequency distribution of wind speeds is a very valuable tool to characterize the wind regime. A narrow distribution implies a relatively constant forcing, such as a katabatic forcing, while a broad range indicates variable synoptic forcing. To facilitate comparison between the distributions at different locations, it is convenient to fit the data to the two-parameter Weibull distribution:

$$F(V) = \frac{\kappa}{\lambda}\left(\frac{V}{\lambda}\right)^{\kappa-1} exp\left(-\left(\frac{V}{\lambda}\right)^{\kappa}\right) \tag{4.2}$$

where $F(V)$ is the frequency distribution of wind speeds, V is the wind speed, κ is the shape parameter and λ is the scale parameter. λ is linearly related to the the annual mean wind speed through:

$$\lambda = \frac{V_{avg}}{\Gamma\left(1+\frac{1}{k}\right)} \tag{4.3}$$

where Γ is the complete gamma function. Hence it is expected that the value of λ will be close to the mean wind speed. The shape of the distribution is relatively wide and right-skewed for $1 < \kappa < 3$, it approximates the normal distribution for $3 < \kappa < 4$, and it is narrow and left-skewed for higher values of κ. The shape factor is more discriminating because it clearly differentiates between variable winds and distributions with long tails (low κ) that are typical of synoptic forcing and narrow distributions (high κ) that correspond to katabatically forced uniform winds.

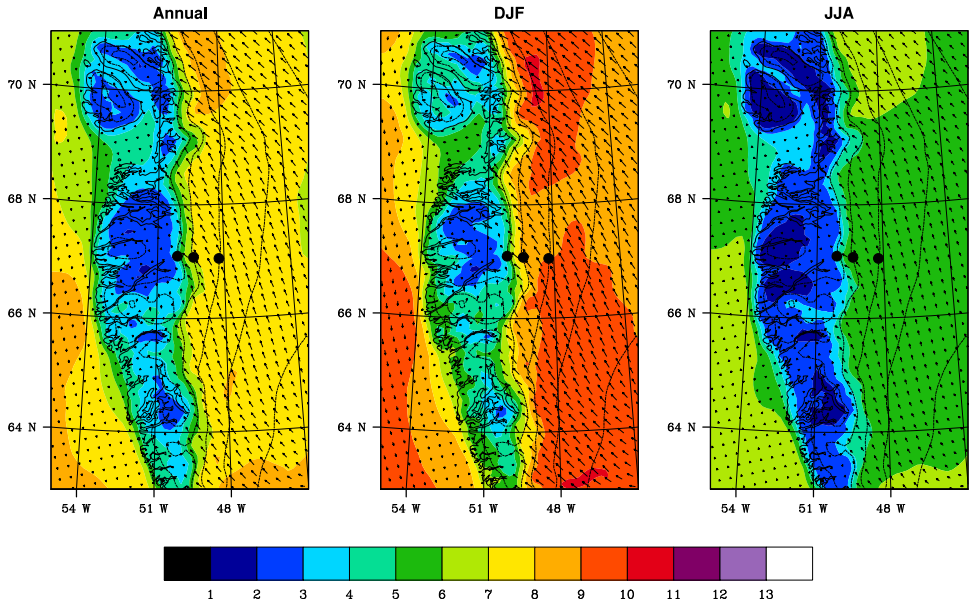

Figure 4.4: 10 m wind (m s^{-1}) near the AWS locations. Wind direction vectors represent vector average wind velocity vector. AWS sites are indicated with black dots. From left to right the panels represent annual average, winter (DJF) average, and summer (JJA) average.

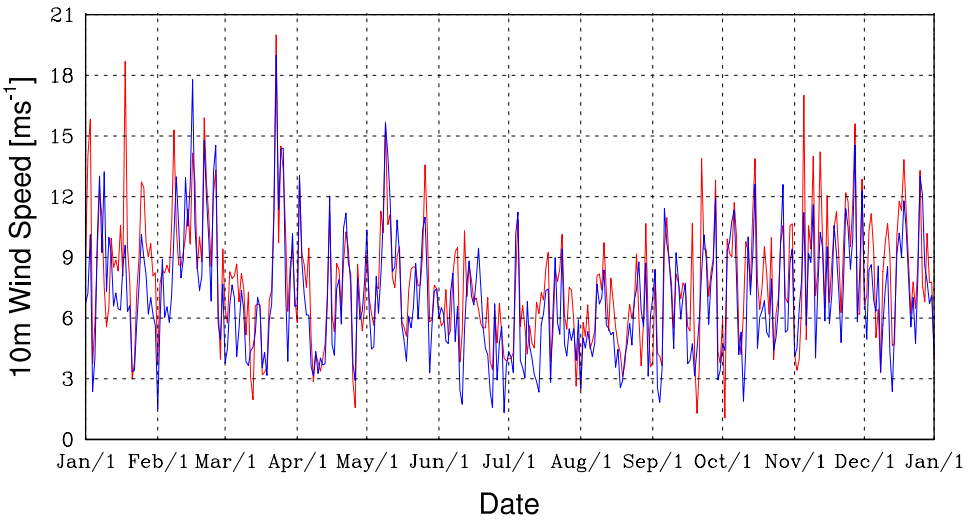

Figure 4.5: Time series of daily average observed (red) and modeled (blue) wind speed (m s^{-1}) at S9 for the year 2004.

To calculate the Weibull parameters, the observed and modeled winds were distributed over 1 m s^{-1} bins from 0 m s^{-1} to 30 m s^{-1}. Many methods exist to determine the Weibull parameters, including maximum likelihood estimation, graphical plotting techniques, method of moments and weighted and unweighted least squares estimation. Each of these methods has its advantages and disadvantages. Lu et al. (2004) present a review of the relevant literature. In the present study, a non-weighted least squares method was chosen for its appealing simplicity and reasonable results. The procedure is described in Al-Fawzan (2000).

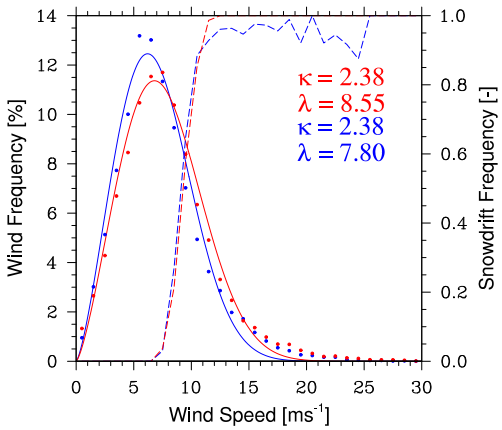

Figure 4.6: Two-parameter Weibull distribution of observed (red) and modeled (blue) wind speeds at S9. Binned data are shown as dots, while the fitted Weibull distribution is shown as a solid line. The estimated (AWS) and modeled (RACMO2) snowdrift frequency is given by the dashed lines.

Figure 4.6 visualizes the procedure. Annually average binned wind speeds are shown as dots, and the corresponding Weibull distribution is fitted. Furthermore, the snowdrift frequency in the snowdrift season is plotted as a function of wind speed. The modeled snowdrift frequency is straightforwardly calculated, but problems arise for the measurements, since no direct observations are available. Therefore, the average threshold friction velocity during the snowdrift season is calculated from model data because the AWS lack snow density measurements. Next, actual friction velocities from the AWS data were calculated and compared to the average threshold friction velocity. This gives a crude estimate of the snowdrift frequency that we expect in the AWS data based on the parameterization used in this research.

It is evident that the shape of the Weibull distribution fits well with the data, but some discrepancies remain. Firstly, both the measured (red) and modeled (blue) fits underestimate the frequency of high wind speeds. This is particularly problematic if the fitted data is used in the calculation of drifting snow, rather than the actual measurements. Here, the distribution was only used as an end product to classify the wind climate. The underestimation of high wind speeds is due to an inherent incapacity of the Weibull distribution to represent the shape of the wind distribution in this region. Experiments performed where the least squares fit was weighted with the snowdrift frequency for each wind speed showed improvement in the high wind region, but qualitatively the same deficiency. Moreover, the fit deteriorated significantly for the lower wind speeds. Interestingly, the shape parameter κ obtained from the model and measurements is identical, while the scale parameter varies. The same result was found for the other two AWS (not shown). Since we are particularly interested in the shape parameter as a means of classifying wind regimes, this result gives further confidence in the ability of the model to represent the wind climate.

The above procedure was applied to the entire model domain. Figure 4.7 shows the average spatial

and seasonal variability of both Weibull parameters for the period 1957-2011. κ varies considerably over the Greenland ice sheet. The relatively low values in the south are indicators of synoptic influence. This is particularly true for the southeast coast, where the Icelandic Low causes strong winds parallel to the coast (Ettema et al., 2010a). Low values of κ are also found along the ice ridge that runs from the southern tip of the ice sheet up the plateau, due to the lack of a significant surface slope and associated katabatic forcing. Over the northern slopes of the ice sheet, extremely high values of κ are found, indicating some of the most uniform winds on earth. A similar pattern of κ was found over Antarctica by Rodrigo et al. (2012), who found the highest values of κ to occur in confluence zones of the katabatic circulation. A closer look at the spatial patterns of κ and the topography suggest that the same argument holds for Greenland. Particularly in the north, the effect is well visible. The values of κ are lower over convex (ridge-like) topography where the katabatic forcing shows considerable diffluence. On the other hand, the highest values are observed in regions where the topography is concave (valley-like), such that the air comes together and accelerates (confluence). Confluence regions occur on large scales (i.e. the three large regions of high κ in the north) and on smaller scales (e.g. near Cape York at $77.5°N, 65°W$). In all cases, topography shows the same pattern, leading to confluence of the katabatic wind. Furthermore, a clear seasonal cycle is visible over the northern part of the ice sheet, with higher values of κ in winter. This is likely due to the stronger katabatic forcing in that season. As expected, the scale parameter λ follows the patterns of the average wind speed shown in Figure 4.2. Small deviations thereof come from different patterns of κ.

To investigate changes in the Greenland wind climate, a trend analysis was performed. To this end, yearly, winter (DJF) and summer (JJA) averages were taken for all years from monthly values of the Weibull parameters. Using a nine-year moving average the short-term variability was removed to reveal the long-term trend. A drawback of using a moving average to calculate the trend is that it is relatively insensitive to values at either end of the time series, such that not all datapoints have equal weights. A simple linear regression ($y = bx + c$) was performed to investigate the behavior of the wind in a changing climate, subject to recent warming. In the presence of a trend, the moving average inevitably yields autocorrelated values, and hence the data are no longer independent, as required by most standard statistical tests. To investigate the significance of the trends the standard t-test must then be modified, because it is otherwise too liberal and rejects the null hypothesis too often. The standard t-test is of the form (Santer et al., 2000):

$$t_b = b/s_b \tag{4.4}$$

where b is the calculated trend and s_b is the standard error of b:

$$s_b^2 = \frac{\frac{1}{n_t-2}\sum_{t=1}^{n_t} e(t)^2}{\sum_{t=1}^{n_t}(t-\bar{t})^2} \tag{4.5}$$

Here, n_t is the number of timesteps, and $e(t)$ is the regression residual at time t. The so obtained value of t_b can be compared with critical value of t from the Student's t-distribution, given significance level α and degrees of freedom $n_t - 2$. Several ways exist to modify the t-test (Zwiers and von Storch, 1995), but the easiest is by defining an equivalent sample size n_e (Zwiers and von Storch, 1995; Santer et al., 2000). Here we define the equivalent sample size with the lag-1 autocorrelation coefficient r_1 (Santer et al., 2000):

$$n_e \approx n_t * \frac{1-r_1}{1+r_1} \tag{4.6}$$

which is valid for large n_t. This effective sample size is now substituted in Equation 4.5 (not in the summation limits), and in the calculation of degrees of freedom. Note that there are more complicated ways of accounting for serial correlation, and that no single definition of the equivalent sample size exists (Zwiers and von Storch, 1995). This method works best for large n_t and $n_e > 30$, which is not always satisfied here. Furthermore, methods that make use of the autocorrelation at longer lags exist. Therefore, the obtained significance merely serves as a first order estimate, but different choices could

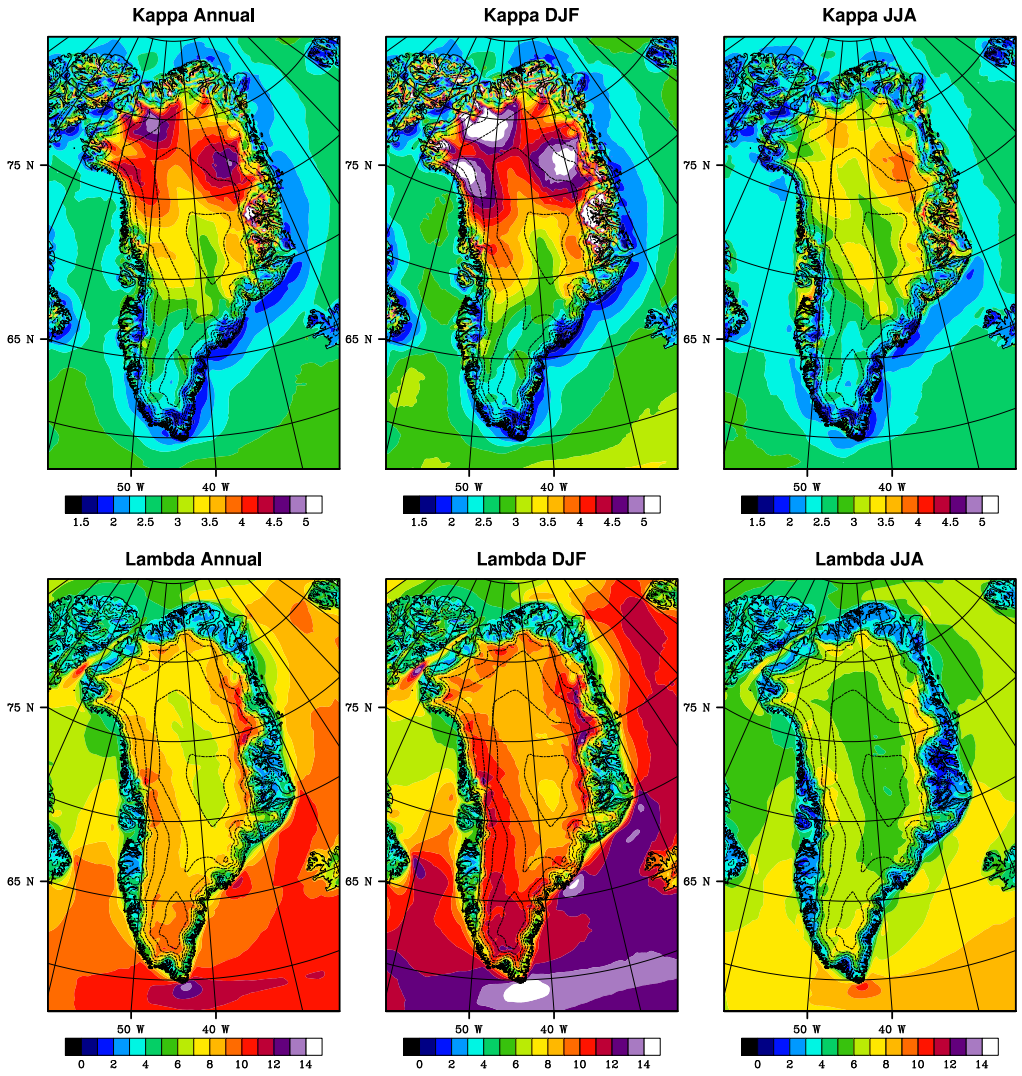

Figure 4.7: Map of Weibull parameters of modeled wind speed. The top three figures show the shape parameter κ (-), the bottom three figures show the scale parameter λ (ms^{-1}). From left two right, figures show the 1957-2011 annual average, winter average and summer average.

have been made.

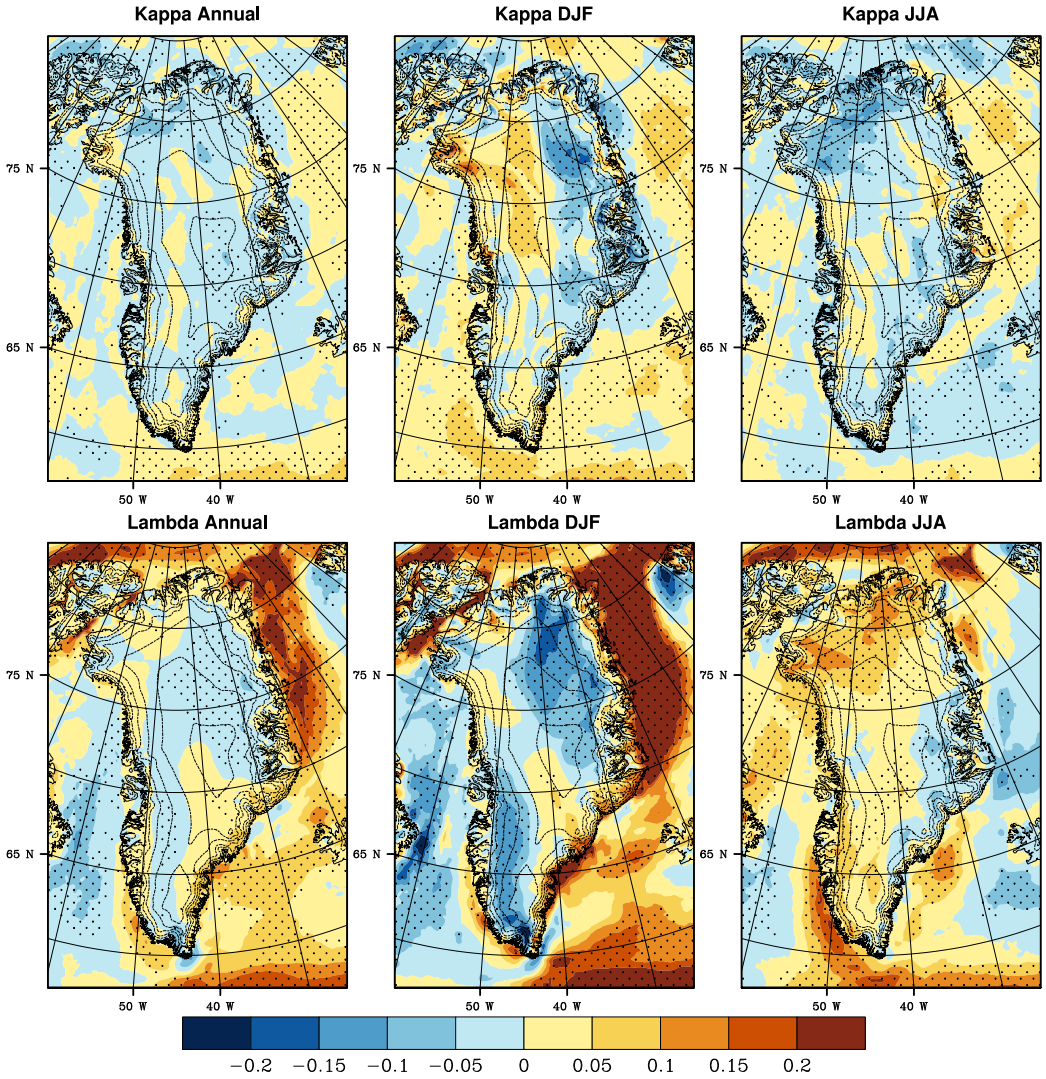

Figure 4.8: 1957-2011 decadal linear trends (change/decade) in the shape (top) and scale (bottom) parameters of the Weibull distribution. From left to right, figures show the trends of the annual, winter and summer averages.

The results of the trend analysis are given in Figure 4.8. For particular locations of interest, the raw data, smoothed data and associated trend lines of both series are given in Figure 4.9. First, it must be noted that trends are generally small and changes in the parameters are of the order of a few percent per decade. Because inter-annual variability is large, a longer time series is needed to statistically prove or reject a significant trend. The shown trends in Figure 4.8 are calculated using a moving average, which is by definition insensitive to the endpoints of the original data series. This has influenced the magnitude of the calculated trend for some locations (e.g. Figure 4.9b). Nevertheless, a trend analysis using the full data series does not change the large-scale patterns observed here.

In the north, the scale parameter κ appears to decrease in summer, suggesting an increased relative importance of synoptic activity. Figure 4.9a illustrates that this decline is gradual and continues throughout the period of investigation. Summer trends of κ are weak over other parts of the ice sheet.

In winter, an unexpected pattern of increased uniformity of the wind is observed in the northwest, while increased synoptic forcing is seen in the northeast. Figure 4.9b highlights the characteristics of this trend in the northeast, and clearly illustrates that the trend is not physical. Instead, the observed trend in this region is a result of large interannual variability, and the insensitivity of the running mean to the beginning and end points of the data series. The increase of κ in the northwest appears to be real (Figure 4.9c).

Trends in the scale parameter λ are stronger and can be divided into four regions of interest. A wintertime decrease of wind speed in the southwest and northeast, an increase in wintertime over sea ice covered regions, and an increase in summer over most of the ice sheet. Closer inspection learns that the wintertime decrease of windspeed in the southwest occurs in the period from the 1980's onwards, that is, in the period of significant warming over the ice sheet (Figure 4.9d). Therefore, it may be related to a reduced winter temperature deficit and reduced katabatic forcing. The decrease of λ in the northeast appears to be linked to the strong increase of the parameter over the sea ice region. The trends in both of these regions stem from a sudden change around 1980 (Figures 4.9e and 4.9f). To rule out the possibility that large changes in the sea ice extent in that period caused these anomalies the prescribed sea ice fields were looked at, but no significant variations were found. Because of the timing of these anomalies it is concluded that this signal is not related to recent warming over the ice sheet, and it is likely linked to multi-decadal variability. Summer values of λ show an increase over almost the entire ice sheet, but particularly in the north, where κ decreases, such that an increased synoptic forcing seems the most probable cause. Here it should be added that a decreasing trend is visible from approximately 1990 (Figure 4.9g), suggesting that the wind climate is changing in response to recent warming.

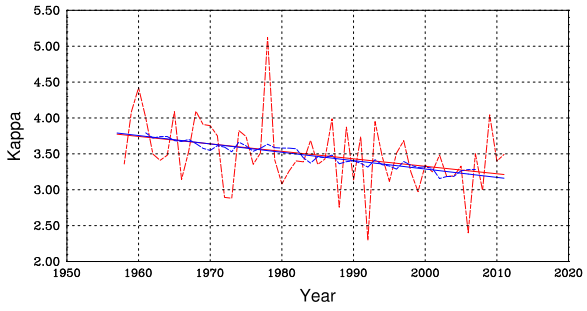

(a) 80°N 50°W: Average JJA κ

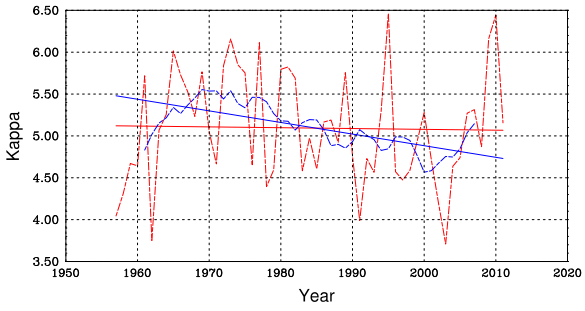

(b) 77.5°N 30°W: Average DJF κ

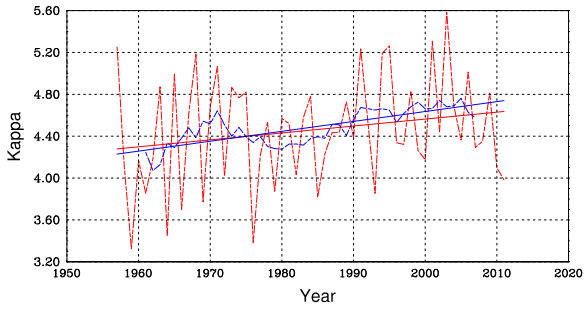

(c) 76.25°N 50°W: Average DJF κ

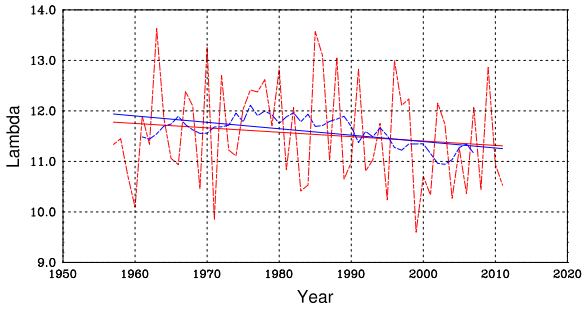

(d) 65°N 48°W: Average DJF λ

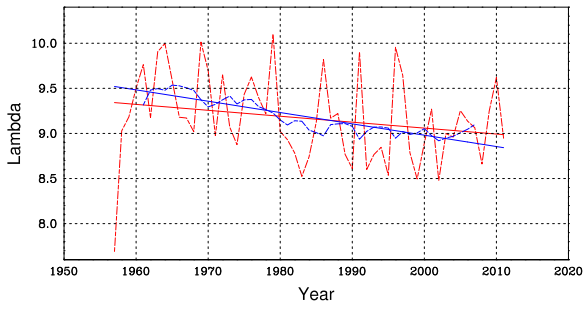

(e) 77.5°N 35°W: Average DJF λ

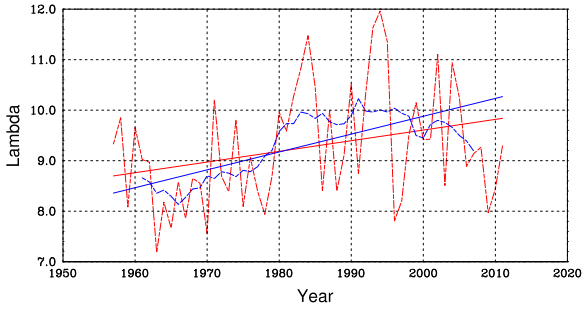

(f) 77.5°N 11°W: Average DJF λ

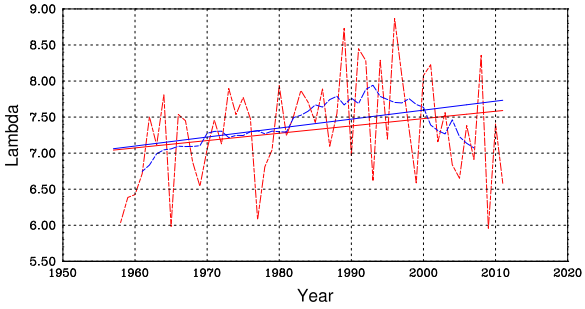

(g) 81°N 40°W: Average JJA λ

Figure 4.9: 1957-2011 trends in the Weibull parameters for locations of interest. The raw data with yearly frequency are given in red; The 9 year moving average thereof is given in blue. The associated linear trend lines are plotted as solid lines.

4.2 Temperature and Humidity

The previous section dealt with characteristics of the wind distribution. This section will cover the temperature and humidity climate of the Greenland ice sheet. Temperature and humidity are closely coupled and crucial to (snowdrift) sublimation rates. Temperature, specific humidity and pressure determine the relative humidity, which in turn limits sublimation. Therefore, it is imperative to look at the temperature and humidity of the ice sheet, and the ability of RACMO2 to simulate these variables.

Figure 4.10 shows the yearly cycle of temperature and specific humidity at S9. As expected, a pronounced seasonal cycle of near-surface temperature is present, forced by absorbed shortwave radiation. In winter, solar radiation is low or absent, and the subsequent radiative energy loss causes a strong temperature inversion near the surface. Depending on the wind speed, turbulent mixing limits the strength of the temperature inversion, such that strong variations of near surface temperature exist. As Figure 4.10 clearly shows, the model is well able to simulate this variability. In summer, variability is much reduced and temperatures fluctuate around the melting point. Firstly, this is caused by the temperature of the surface that cannot rise above the melting point. Hence, when temperature rises above the melting point, the surface has a cooling effect on the overlying atmosphere through a downward sensible heat flux. Furthermore, no strong temperature inversion exists in summer and the effect of mixing on the near surface temperature is much reduced. Similar to the results shown here, but extended for a much larger network of AWS, Ettema et al. (2010b) found good agreement between RACMO2 and measurements. They found a small (-1.5°C) cold bias over seasonally snow covered land, and a small ($+0.9$°C) warm bias over the ice sheet. Here the results may be expected to be slightly improved, due to a new albedo parameterization and the inclusion of a snowdrift routine, but no extensive evaluation was performed.

The seasonal cycle of specific humidity is shown in Figure 4.10b and shows a clear resemblance to Figure 4.10a. Moisture content of the atmosphere is high in summer, when temperatures are high and the atmosphere can hold more moisture. Again RACMO2 is able to realistically simulate variability on the timescale of days.

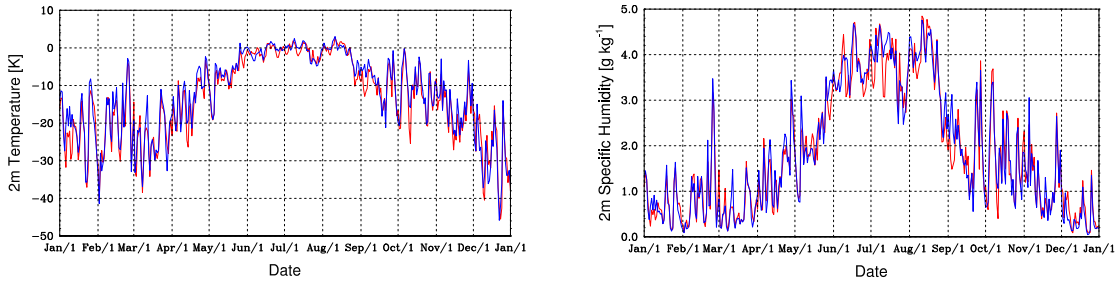

(a) Daily average temperature (°C)

(b) Daily average specific humidity (g kg^{-1})

Figure 4.10: Time series of measured (red) and modeled (blue) daily average values of temperature and specific humidity at S9 for the year 2004.

Spatial patterns of temperature and specific humidity are shown in Figures 4.11 and 4.12 respectively. The strong seasonal cycle is present over the entire ice sheet. The spatial pattern of temperature consists of two main signals. Firstly, temperatures decrease towards the north(west), owing to the global meridional temperature gradient, sea surface temperatures and the presence of sea ice. The latter factor can clearly be seen to the northeast of the Greenland ice sheet. Secondly, temperature decreases from the margin of the Greenland ice sheet to its center. This pattern is explained by the increasing elevation of the ice sheet towards its center, and the corresponding lower atmospheric temperatures. This pattern is weakest in summer, because temperatures at the margin are limited by the

temperature of the melting surface. Temperatures only reach values well above the melting point over the ice free tundra. This figure adequately shows why the ablation zone is so narrow. Over most of the ice sheet the daily average temperature is well below the freezing point, even in summer, when the sun is above the horizon all day. Surface melt is therefore rare or absent in the interior of the ice sheet.

Again, specific humidity closely follows the temperature patterns. Extremely dry air is found in the interior of the ice sheet. This is mainly due to the extremely low temperatures, limiting moisture content of the atmosphere, but also due to the large scale circulation pattern. Divergent katabatic winds over the ice sheet cause subsidence over the interior of the ice sheet, such that the air is replenished with dry air from higher in the atmosphere. This circulation pattern limits the near surface transport of moist air from the ocean up the ice sheet (Dethloff et al., 2002).

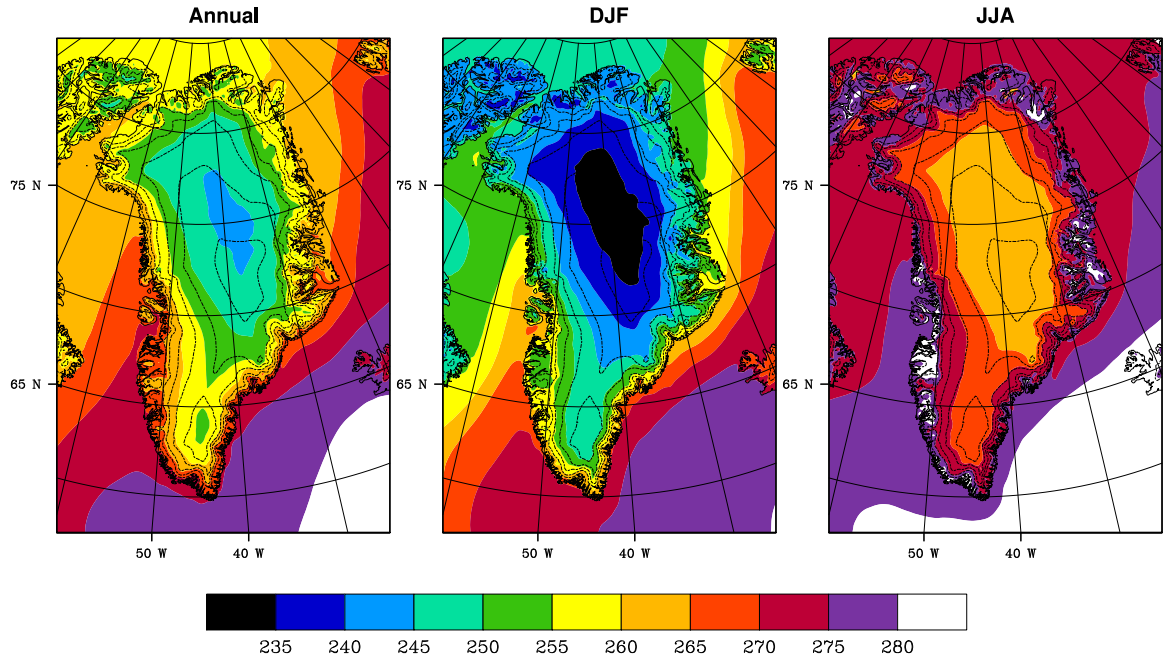

Figure 4.11: Map of 1957-2011 average annual (left), winter (middle) and summer (right) temperature (K).

Though interesting in their own right, the description of temperature and humidity served to understand the snowdrift climate. Sublimation of drifting snow is proportional to the undersaturation of the air, and thus depends on relative humidity. Following WMO (World Meteorological Organization) convention, the standard processing of relative humidity by RACMO2 calculates the ratio of the actual water vapor pressure to the saturation water vapor pressure over liquid water, or relative humidity with respect to water (RH_w hereafter). Similarly, the AWS store data as RH_w by default. However, at subfreezing temperatures the saturation water vapor pressure over ice is lower than that over water, and so the air is saturated with respect to ice sooner than to water. Relative humidity with respect to ice (RH_i hereafter) is therefore a more appropriate measure. The AWS relative humidity was processed using a two step scheme that is used for all AWS operated by IMAU. Firstly, RH_w was converted to RH_i by multiplying it with the ratio es_w/es_i using the expression of Curry and Webster (1999), in the form presented by Van den Broeke et al. (2004). Secondly, for $T < -20°C$ the data still are too low, because this is outside the instruments temperature calibration range. To resolve this, a polynomial function is fitted to the 98th percentile, which is used to rescale the data such that 2% of the values

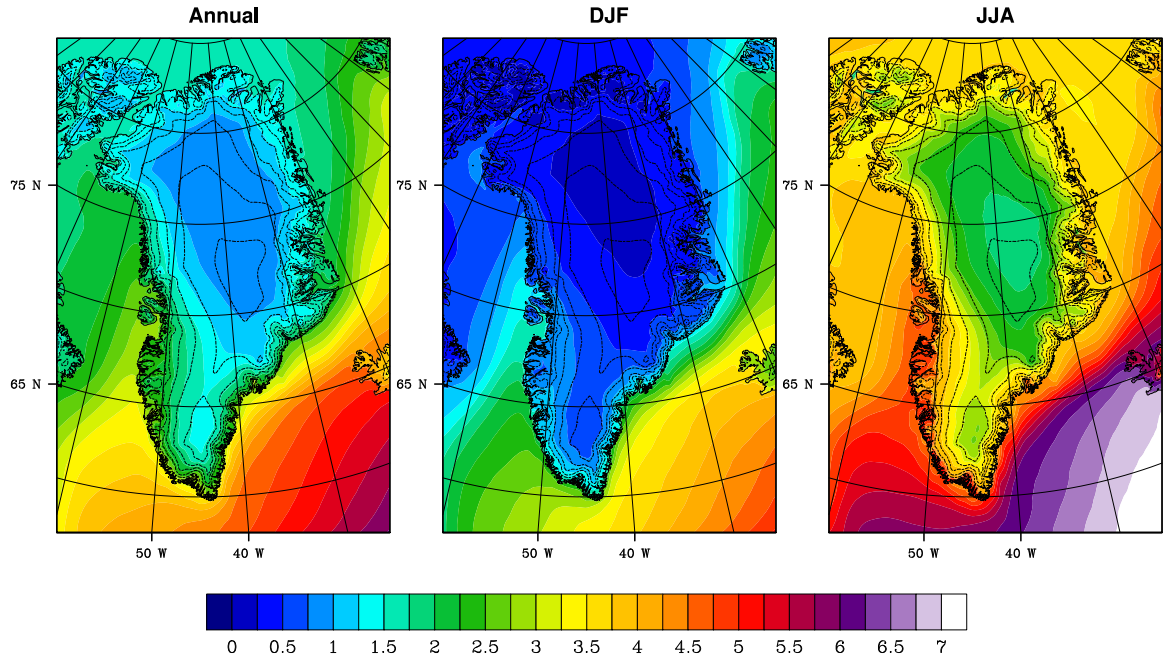

Figure 4.12: Map of 1957-2011 average annual (left), winter (middle) and summer (right) specific humidity (g kg^{-1}).

are above 100% RH_i (Van den Broeke et al., 2004). For RACMO2 data, a slightly simpler procedure was used. Instead of correcting RH_w, RH_i was calculated from the specific humidity, the temperature and the surface pressure using the Goff Gratch equation for saturation vapor pressure over ice. The second correction step was not performed, because it is associated with instrument calibration, which is not applicable to the model output.

Figure 4.13 shows the yearly cycle of RH_i at S9. Measured values are close to saturation year-round. Modeled values show a reasonably similar pattern, although in winter variability is overestimated and a negative model bias persists. This effect is even more pronounced at S6 (not shown), but less so at S5. Part of the explanation may be in the upward correction scheme of the observations that is used at low temperatures. Overall, the discrepancy between model and measurements is larger than for temperature and specific humidity.

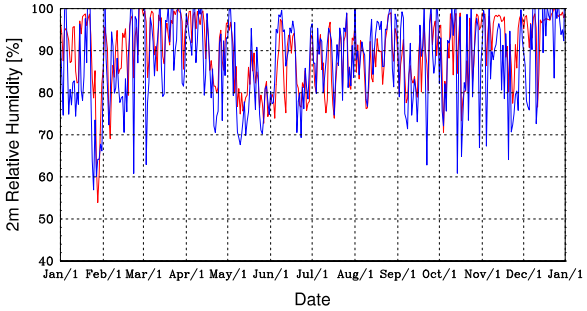

Figure 4.13: Time series of daily average relative (%) humidity over the year 2004 at S9

The spatial distribution of RH_i is presented in Figure 4.14. As in Figure 4.13, a seasonal cycle is visible. A different feature that persists throughout the year is a decrease of relative humidity towards the ice sheet margin. A possible explanation is that the near surface wind pattern transports very cold and dry air from the interior towards the lower elevations, and that associated adiabatic heating reduces the relative humidity of the air (Ettema et al., 2010b). In the very cold regions at high elevations supersaturation regularly occurs and average RH_i is above 100%.

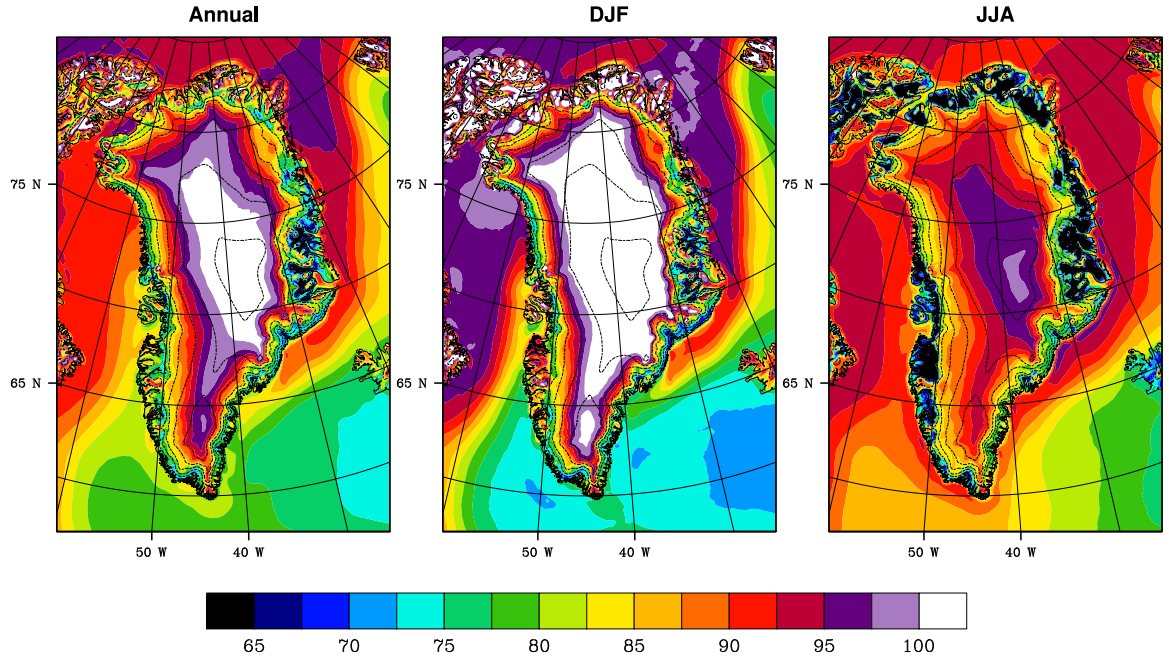

Figure 4.14: Map of 1957-2011 average annual (left), winter (middle) and summer (right) relative humidity.

Another particularly insightful way to present the relative humidity is to plot it as a function of wind speed. The result is shown in Figure 4.15. These results clearly show three different wind regimes. First, a low wind ($V < 5 m\ s^{-1}$) regime exists where relative humidity is high. Second, as wind speeds pick up, relative humidity decreases significantly. Then, with the (estimated) onset of snowdrift this drop stabilizes and for high wind speeds relative humidity increases to saturation again, which represents the third (high) wind regime.

In the neutral or stable boundary layer over the Greenland ice sheet, the first (low) wind regime is explained by the lack of turbulent mixing in the absence of wind. If this occurs in winter, a strong temperature inversion develops at the surface such that the saturation vapor pressure decreases sharply and saturation of the near surface air results. If this occurs in summer, either sublimation or evaporation will add moisture to the near surface air, and in the absence of mixing this will result in saturation. With increasing wind speeds, vertical turbulent exchange mixes the near surface air with that of higher layers. In winter, this limits the development of a strong temperature inversion because warmer air is mixed into the surface layer. In summer, the moisture flux into the surface layer is diffused over the boundary layer and saturation of the near-surface air is therefore limited. With the onset of snowdrift, the moisture flux into the atmosphere is increased significantly (Bintanja, 2000b), and simultaneously the air is cooled by a downward sensible heat flux. The result is that relative humidity increases if snowdrift occurs.

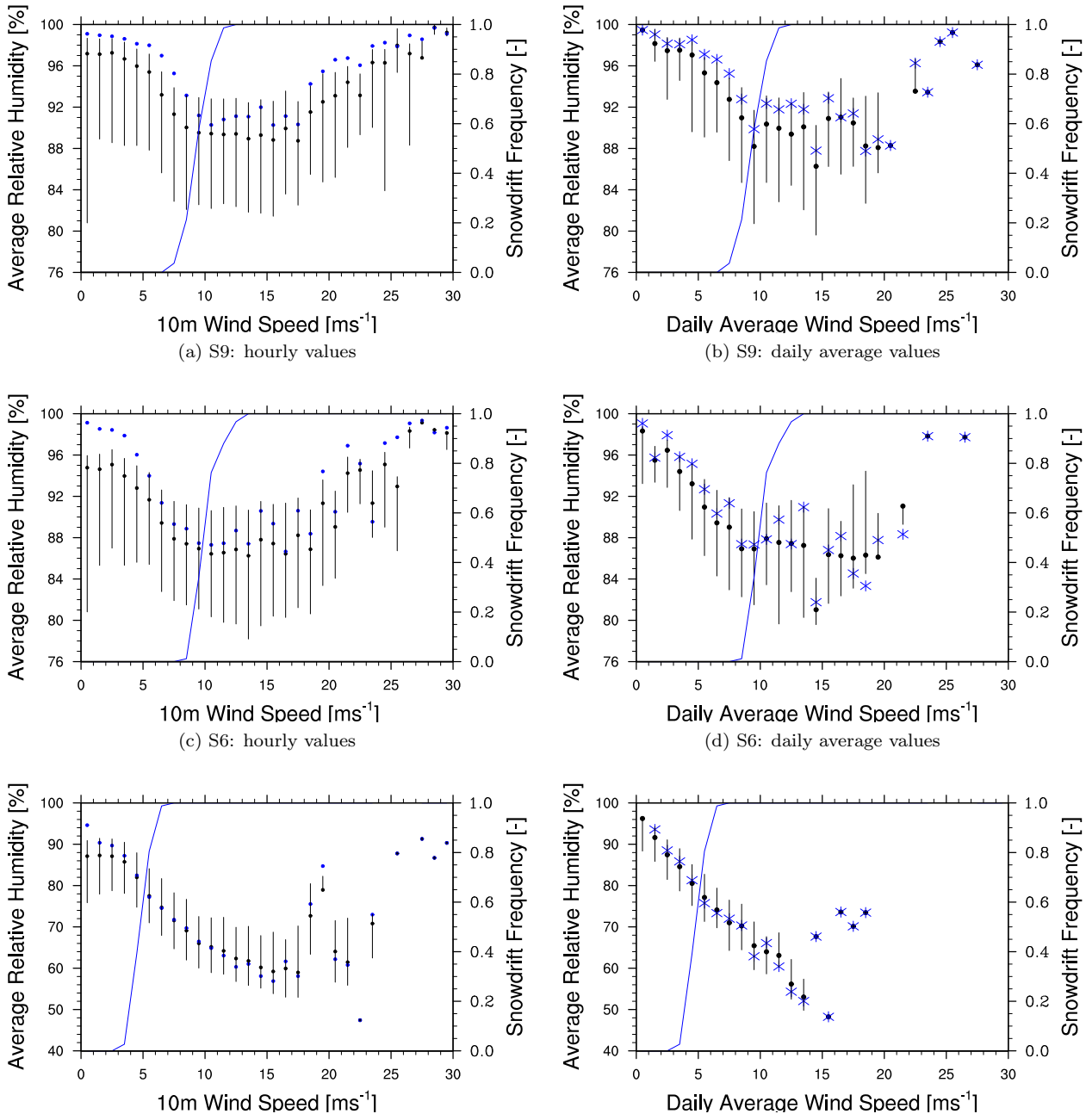

(a) S9: hourly values

(b) S9: daily average values

(c) S6: hourly values

(d) S6: daily average values

(e) S5: hourly values

(f) S5: daily average values

Figure 4.15: Relative humidity at 2 m at the three AWS as a function of 10 m wind speed during the snowdrift season (October-April). Shown are average relative humidity (black dots) and median relative humidity (blue dots / crosses). The spread is indicated by the black lines, that represent the standard deviation of the collection of points above and below the mean respectively. Measurements are daily averages or instantaneous hourly values over the period 2003-2010. Estimated snowdrift frequency (October-April) as a function of windspeed is shown as a blue line.

These features are clearly visible at S9, as shown in Figure 4.15a. The onset of snowdrift appears to correspond well with the stabilization of relative humidity. In this stable region, snowdrift is likely limited. The real increase of relative humidity only occurs at high wind speeds of roughly 20 m s^{-1} or higher. Apparently it is only at these high wind speeds that the moisture flux at 2 m is large enough to cause saturation. It is interesting to see if the time it takes for such a snowdrift layer to develop influences the results. Figures 4.15a, 4.15c and 4.15e show instantaneous values 10 m wind speed and 2 m relative humidity. Here it may occur that the wind speed is large, but that the snowdrift layer has yet to reach the measurement height of relative humidity, such that low relative humidity is measured regardless of the high wind speed and the occurrence of snowdrift. In that case, the effect can be expected to be more pronounced when relative humidity at 6 m is used instead. This was investigated but no difference was found. As a further check, daily averages were used instead of instantaneous values. On the timescale of a day, the development time of the drifting snow layer is believed not to be a limiting factor. These results are shown in Figures 4.15b, 4.15d and 4.15f. Qualitatively, the same results are found, which leads to the conclusion that the time needed for the development of the snowdrift layer is of minor importance for measurements at 2 and 6 m heights.

To understand the processes at work during a snowdrift event, and as a final validation of RACMO2, a detailed look at one particular snowdrift event is presented in Figures 4.16 and 4.17. An extreme event is presented with 10 m wind speeds exceeding 30 m s^{-1} on two occasions within two days and wind speeds continuously over 15 m s^{-1}. There is a very large vertical wind speed gradient during these events, meaning that turbulence is strong. This is immediately reflected in the 2 m temperature, which is increased due to intense mixing. The specific humidity follows the temperature profile closely, meaning that a lot of moisture must be added to the atmosphere or mixed downward from higher layers. The close relation between temperature and specific humidity is confirmed by the relative humidity which rapidly increases to saturation at the onset of the snowdrift event and remains there. The similarity in the value and response of the relative humidity curves at 2 and 6 m further seem to suggest that the growth of the snowdrift layer happens fast.

The model results of this event show considerable difference with the measurements. The first wind event is not picked up by the model, but the second one is relatively well represented, considering the lower temporal resolution of the model. The fact that the model misses some high wind events was known, but in general the model captures most events (e.g. Figure 4.5). The temperature response of the model closely follows observations, although there appears to be a significant warm bias. The resemblance of the temperature response of model and measurements is even reasonable during the first wind event, which is not captured by RACMO2. A likely explanation thereof may be that mixing is strong in either case, since modeled winds during the event still exceed 20 m s^{-1}. The response of specific humidity is reasonably represented, indicating that mixing and (average) snowdrift sublimation are well captured. However, the modeled RH_i (solid) and RH_w (dashed) show hardly any resemblance to the measurements. Part of the explanation may be in the positive temperature bias. The snowdrift parameters SU_{ds} and TR_{ds} show nearly identical time series and are clearly dominated by the modeled wind speed.

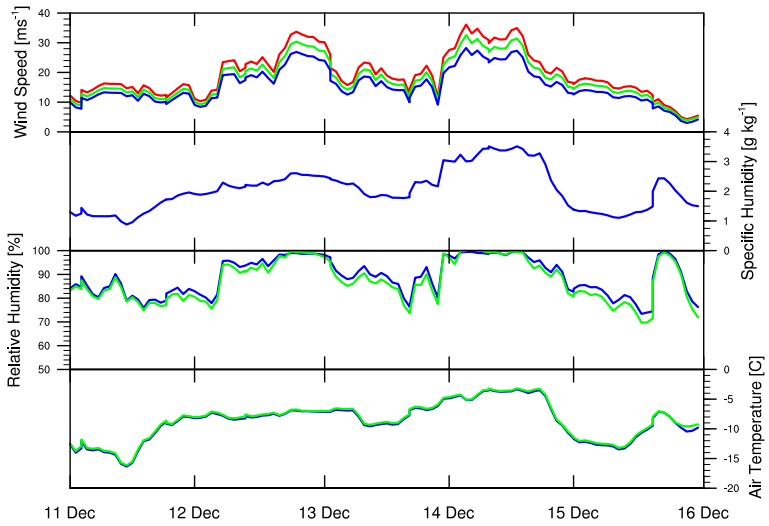

Figure 4.16: Time series of hourly observations of wind, humidity and temperature at 10 m (red), 6 m (green) and 2 m (blue) height during a snowdrift event in 2009.

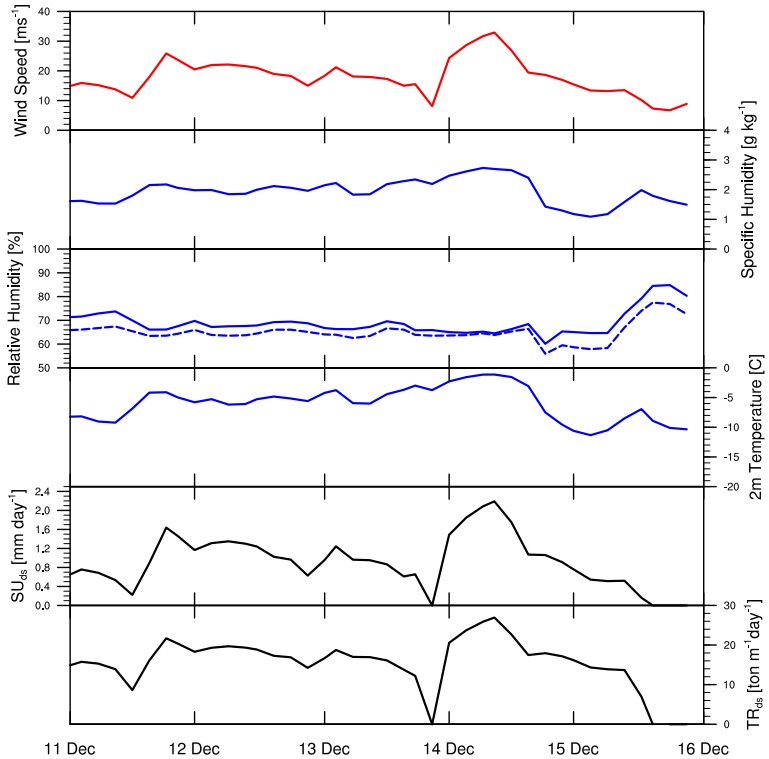

Figure 4.17: Time series of 3 hourly modeled values of wind, humidity, temperature and snowdrift parameters during a snowdrift event in 2009. Results at 10 m height are given in red, results at 2 m height are given in blue. No accurate heights exist for the snowdrift parameters which are therefore given in black. Relative humidity with respect to water is given as a dashed line.

4.3 Snowdrift

Now that the wind, humidity and temperature climate of the Greenland ice sheet have been analyzed, it is interesting to look at the snowdrift parameters directly with the use of RACMO2 model data. Snowdrift evidently depends on the amount and type of snow present. Therefore, Figure 4.18 shows annual average snowfall rate and surface density. Snowfall rates are lowest in the north, where low temperatures limit moisture content in the near-surface atmosphere. In the south, snowfall rates are much higher, particularly in the southeast where the Icelandic Low causes flow of air towards the ice sheet. Snowfall over the Greenland ice sheet is dominated by orographic lifting and frontal precipitation, which explains the observed pattern of precipitation. Surface snow density is shown in Figure 4.18b and is clearly influenced by melt. Furthermore, the density of fresh snow depends on the temperature and atmospheric conditions where it falls. Near the margins of the ice sheet, the occurrence of melt increases the densification rate of the snowpack (Ligtenberg et al., 2011). The effect of increasing surface density on the threshold friction velocity for snowdrift is quantified by Lenaerts et al. (2012a), who calculate that for a density increase from 300 to 500 kg m^{-3}, the increase in friction velocity is from 0.4 to 1.2 m s^{-1}, the latter corresponding to a wind velocity of over 30 m s^{-1} at 10 m above the surface.

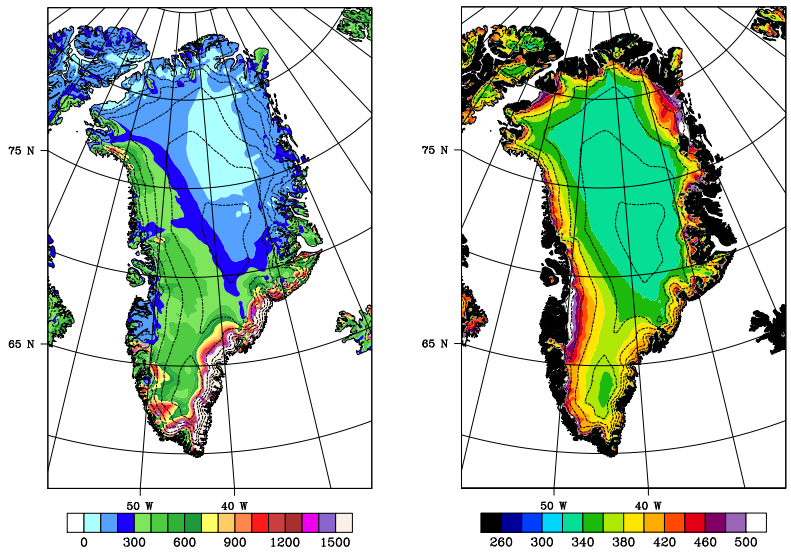

(a) Snowfall [mm $year^{-1}$] (b) Surface Density [kg m^{-3}]

Figure 4.18: Map of 1957-2011 annual average values of snowfall (a) and surface snow density (b).

The resulting spatial patterns of drifting snow are presented in Figure 4.19. Drifting snow frequency is defined as the percentage of days with integrated snowdrift transport of more than 3 kg m^{-1}. Drifting snow can be found anywhere on the ice sheet, with frequencies ranging from 20% in the high interior, to 70% or higher in the northeast in Dronning Louise Land. The pattern of snowdrift frequency strongly resembles that of (winter) wind speed. The regions of most frequent snowdrift are the southeast, northeast and western coasts, where winds are strongest and surface densities are relatively low (Lenaerts et al., 2012b). Snowdrift transport shows a similar pattern as snowdrift frequency. Transport rates as large as 2 kt $m^{-1}y^{-1}$ are observed in the northeast, while transport rates of only 0.3 kt $m^{-1}y^{-1}$ are found in the interior. Over the tundra, hardly any transport occurs due to the low wind speeds.

Snowdrift transport acts to redistribute snow over the ice sheet. Snow is picked up on one particular

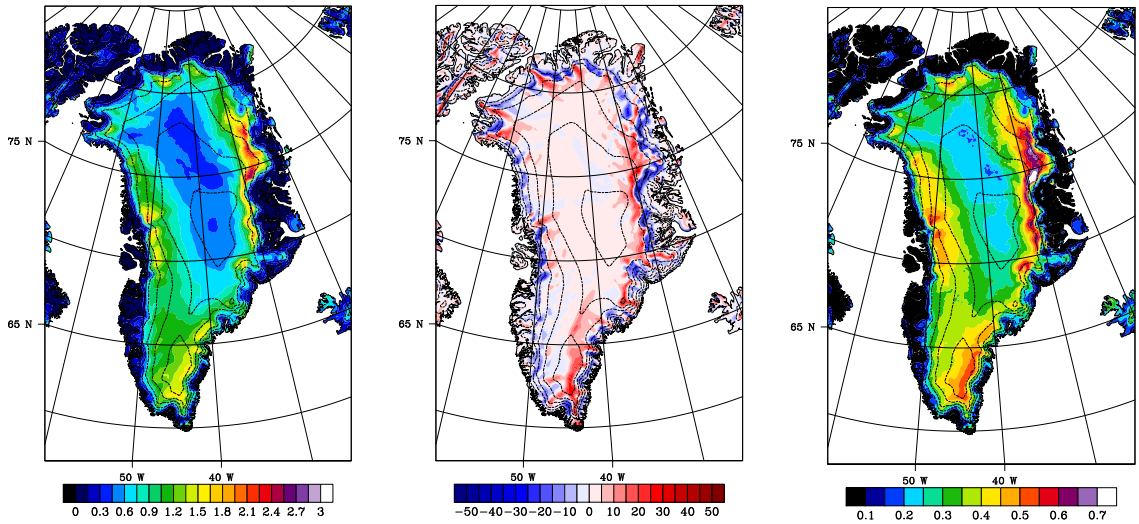

(a) Snowdrift Transport [kt m^{-1} y^{-1}] (b) Snowdrift Erosion [mm $year^{-1}$] (c) Snowdrift Frequency [-]

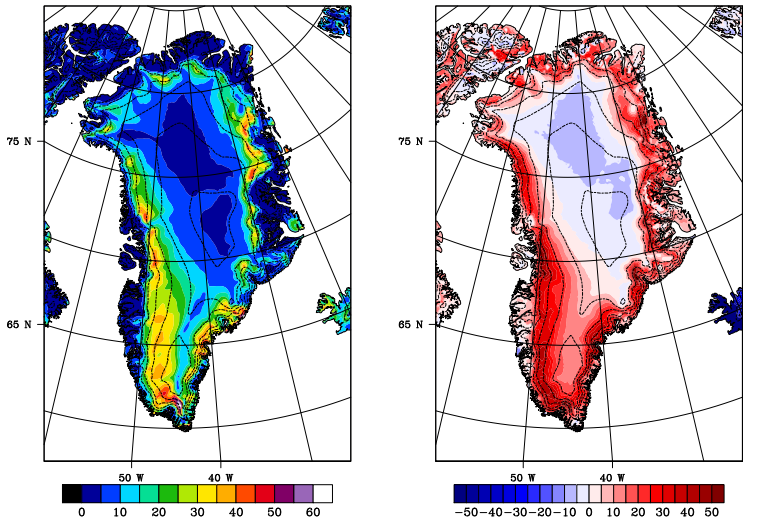

(d) Snowdrift Sublimation [mm $year^{-1}$] (e) Surface Sublimation [mm $year^{-1}$]

Figure 4.19: Map of 1957-2011 annual average values of snowdrift transport (a), snowdrift erosion (b), snowdrift frequency (c), snowdrift sublimation (d) and surface sublimation (e).

location, transported elsewhere, and if not sublimated, it will be deposited. The local erosion rates are calculated as the divergence of the transport vector and shown in Figure 4.19b. Divergence of transport occurs in regions where the wind speeds up, either in response to increased katabatic forcing or in response to confluence. This is the case in the region from the centre of the ice sheet towards the coast. Here local erosion due to snowdrift occurs. Closer to the coast, the katabatic wind decelerates due to thermal forcing or diffluence, and the snow is deposited. Both erosion and deposition of the snowdrift transport vector are strongly topographically determined. A minor contribution to the mass balance is the loss of blowing snow due to deposition over the ocean (Lenaerts et al., 2012b).

Absolute mass loss due to snowdrift sublimation is presented in Figure 4.19d. Snowdrift sublimation is remarkably high along the west coast, when compared to snowdrift transport in this region. This

effect likely has to do with the fact that snowdrift sublimation is proportional to temperature, which is markedly higher in that region than in the northeast. However, the relative importance to the mass budget is larger in the northeast, due to the lower snowfall rates. There, snowdrift sublimation removes over 25% of annual average snowfall, while in the southwest this is limited to roughly 10% (not shown). Integrated over the entire ice sheet snowdrift sublimation accounts for 7% of total ablation (Lenaerts et al., 2012b).

Annual average surface sublimation is clearly linked to temperature. Deposition occurs in the cold regions in the north or high on the ice sheet. Low temperatures cause a low saturation vapor pressure over ice in those regions, such that the air is supersaturated with respect to ice and deposition occurs. In the warmer regions sublimation occurs when temperatures are still below the melting point. Surface sublimation is of similar magnitude as snowdrift sublimation, but while mass loss due to sublimation occurs mostly in summer, snowdrift sublimation occurs mostly in winter. Surface sublimation contributes 40% to total sublimation, while snowdrift sublimation contributes 60%. The inclusion of a snowdrift routine to the model has increased total sublimation with 40%, but reduces surface sublimation with the same percentage (Lenaerts et al., 2012b).

The seasonal cycle of sublimation is shown in Figure 4.20 for three locations on the ice sheet. Snowdrift sublimation is strong in winter, but diminishes at all locations in summer. SU_s is large in summer, and negative in winter on all locations. These results further illustrate the large regional differences on the Greenland ice sheet. SU_{ds} is largest in the K-transect region, even though snowdrift frequencies are larger in the northeast. In the dry interior of the ice sheet drifting snow is relatively rare, and due to low temperatures and high relative humidity sublimation is low. The seasonal cycle of SU_s nicely shows the length of the cold season. In the interior, significant deposition occurs nearly year-round, while in the K-transect region the length of the deposition period is as long as the length of the sublimation period. The northeast shows intermediate values.

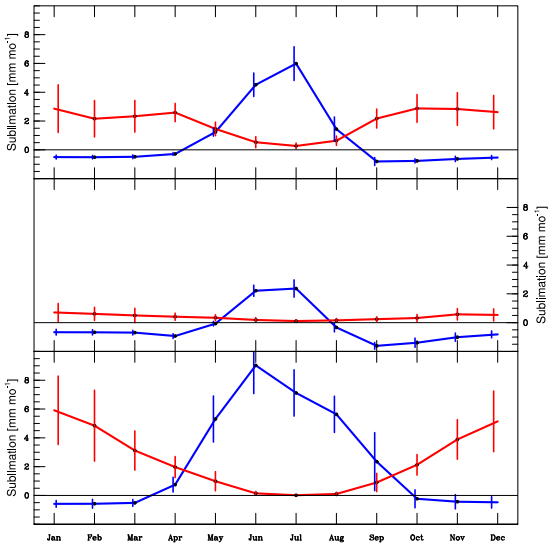

Figure 4.20: Annual cycle of drifting snow and surface sublimation. The upper figure represent snowdrift region in the Northeast, the middle represents the low snowdrift zone in the interior of the ice sheet, and the bottom one shows the Southwest K-transect region.

5 Changes in the Climate of the Greenland Ice Sheet

The previous chapter has presented the climate of the Greenland ice sheet with the use of AWS data from 2003-2010 and RACMO2 data for the period 1957-2011. This chapter will investigate the changes in the Greenland climate in response to global climate change. In particular, it will investigate the differences between the climate of the last two decades (1979-1998) of the 20^{th} century with the simulated climate of the last two decades (2079-2098) of the 21^{th} century.

Before proceeding to the actual results, a discussion of some complexities is appropriate. For all results of the previous chapter, a model run was used that was forced at the lateral boundaries by ECMWF reanalyses. The ECMWF data from ERA-40 (1957-1988) and ERA-interim (1989-2011) are gridded reanalyses of observational data. This lateral forcing with observational data limits the deviation of the model from reality, and so it is the most reliable to characterize the Greenland climate. This run will be referred to as the *climate run* (or CLRUN) hereafter. For future simulations this forcing based on observations is not available, and the model can be expected to behave differently. Instead the model is forced with output from a *General Circulation Model* (GCM).

A comparison of the GCM-forced model run with the reanalysis-forced run can therefore show climate differences that are due to the different setup of the model run, rather than differences in the actual climate. To circumvent this problem, the 20^{th} century climate was reevaluated using a GCM-forced run (*historical run* or 'hist' hereafter). Comparison of this model run with future simulations should not be hindered by differences in the model setup. Here, output from the HadGEM2 General Circulation Model was used.

Simulation of the future climate requires assumptions on how the climate will change. Several scenarios of future climate change that were developed by the scientific community were selected by the IPCC to serve as plausible future pathways "compatible with the full range of stabilization, mitigation and baseline emission scenarios available in current scientific literature" (Moss et al., 2008). These so called *representative concentration pathways* prescribe the evolution of the concentration of greenhouse gasses in the atmosphere, and the associated radiative forcing. Here, an intermediate scenario was chosen that stabilizes concentrations and radiative forcing at 4.5 Wm^{-2} in 2100. For future simulations the model was forced with greenhouse gas concentrations as prescribed by this scenario (RCP45 hereafter) and sea ice and sea surface temperature from HadGEM2 simulations.

5.1 Seasonal patterns of change

To evaluate the performance of the historical run in comparison to the ERA forced climate run, the seasonal cycle of key variables is shown in Figures 5.1 and 5.2. The historical run (blue) realistically simulates the seasonal cycle of temperature, and shows only minor deviations from the climate run (black). Moreover, interannual variability is properly represented, suggesting that the GCM provides a realistic forcing at the lateral boundaries. Similarly, the seasonal cycle of the 10 m wind is generally well represented, although a small negative bias exists in summer. Snowdrift frequency and transport are slightly underestimated in summer. This negative bias may have to do with the underestimation of

wind during that period, and to the small overestimation of near-surface temperature in early summer. Snowfall is, on average, correctly modeled, but the large interannual variability limits conclusive statements on the differences. It appears that snowfall is underestimated in summer, but overestimated in fall. Again, overestimated early summer temperatures may explain some of the difference. However, a longer time series is needed to make more precise statements on seasonal biases of the historical run. Meltwater runoff is again overestimated in early summer, strengthening the hypothesis that positive temperature bias in that period influences the results. Meltwater runoff will increase in response to overestimated temperatures for two reasons. First, more energy will be available for melt. Second, the increased fraction of liquid precipitation will often directly add to the runoff flux or increase the heat content of the snowpack if it refreezes. Sublimation variables SU_s and SU_{ds} are well represented.

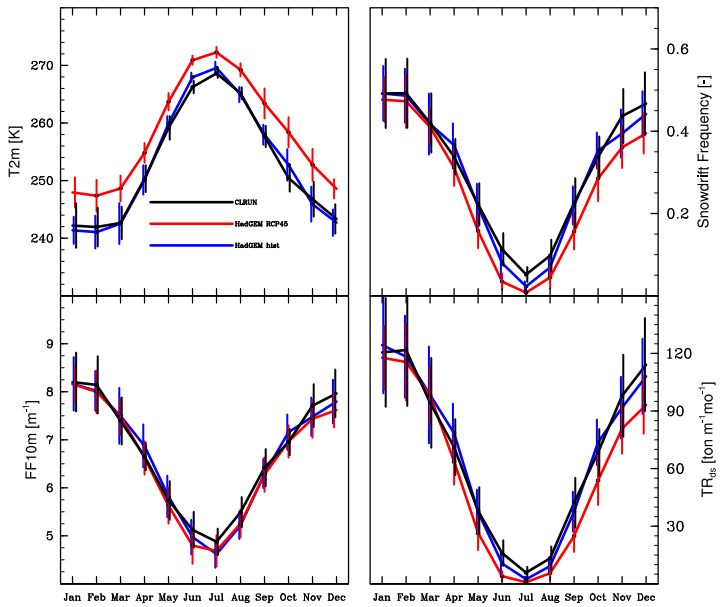

Figure 5.1: Annual cycle of the near surface climate of the Greenland ice sheet. The climate run is presented in black, the historical run in blue, and the RCP45 run in red.

	CLRUN	hist	RCP45
SU_s	20±2 Gt yr^{-1}	20±2 Gt yr^{-1}	18±3 Gt yr^{-1}
SU_{ds}	27±3 Gt yr^{-1}	26±3 Gt yr^{-1}	25±2 Gt yr^{-1}
TR_{ds}	803±60 ton m^{-1}yr^{-1}	790±67 ton m^{-1}yr^{-1}	684±43 ton m^{-1}yr^{-1}
PR_{solid}	903±74 Gt yr^{-1}	879±119 Gt yr^{-1}	1007±74 Gt yr^{-1}
RU	412±87 Gt yr^{-1}	593±127 Gt yr^{-1}	1500±217 Gt yr^{-1}
$T2m$	253±1 °C	252±1 °C	258±1 °C
$w10m$	6.72±0.11 ms^{-1}	6.66±0.16 ms^{-1}	6.58±0.11 ms^{-1}

Table 5.1: Annual average spatially integrated values of different runs. Uncertainty indicates the standard deviation of interannual variability.

Some differences aside, the historical run generally performs well and resembles the climate run. This justifies an investigation of the response of the ice sheet to future climate change using the GCM-

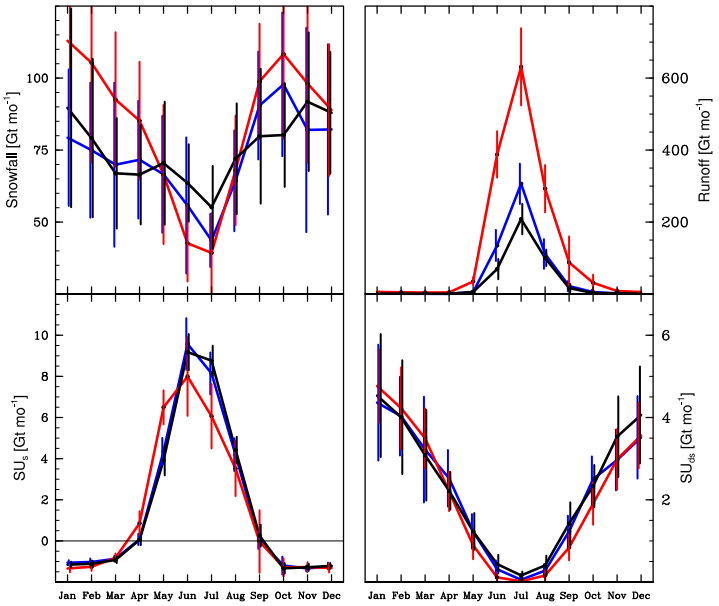

Figure 5.2: Annual cycle of the mass balance of the Greenland ice sheet. The climate run is presented in black, the historical run in blue, and the RCP45 run in red.

forced runs. Figures 5.1 and 5.2 also show the simulated seasonal cycle of these variables of the RCP45 run (red). Table 5.1 provides an overview of the annual averages and interannual variability of the different runs.

The model shows a pronounced temperature increase of roughly 6 K over the ice sheet at the end of the 21st century. A temperature rise was expected, since the model was forced with a scenario of moderately increased radiative forcing. Nevertheless, a temperature rise of 6 K is significantly larger than the projected global temperature change, highlighting the amplifying climate feedbacks in the Arctic region. The temperature increase is largest in winter, because the near-surface temperatures in summer are limited by the temperature of the melting snow surface. The wind speed is surprisingly stable in comparison to the large temperature increases. Averaged over the ice sheet the annual average wind speed decreases from 6.66±0.16 ms^{-1} to 6.58±0.11 ms^{-1}. From Figure 5.1 it becomes clear that this decrease is most evident in spring and early summer. In response to changes in both the wind and temperature climate, transport of drifting snow decreases throughout the year. Raised temperatures increase the rate of snow metamorphism, such that the density and cohesiveness of the snowpack increase faster. This raises the threshold friction velocity and limits drifting snow during the snowdrift season, but furthermore the length of the melting season is increased, during which no snowdrift occurs. The results is a 13% decrease of snowdrift transport averaged over the ice sheet. Considering the year-round nature of this decrease, temperature, rather than wind speed, is the dominant cause of this change.

The accumulation in the form of snowfall will increase significantly in winter, due to the larger moisture holding capacity of the atmosphere. In summer however, snowfall decreases because of the increasing percentage of liquid precipitation in a warming climate (Ettema et al., 2009), such that total precipitation will still increase. Nevertheless, an regional increase in snowfall can be expected even in summer in areas where the near-surface temperatures remain below the freezing point. The decrease of snowfall will consequently be limited to the near-coastal zone. Averaged over the ice sheet, a snowfall increase of 15% will add over 100 Gt yr^{-1} of mass to the Greenland ice sheet annually.

A remarkable increase of 153% in annual average meltwater runoff is observed, equivalent to 907 Gt yr^{-1}, or roughly 3 mm yr^{-1} of eustatic sea level rise. The length of the melt season is significantly increased, and melt rates more than double for all months. The enormous increase in meltwater runoff is predominantly caused by increases in the melt season and melt area. However, a small contribution is expected to come from the increased amount of liquid precipitation that falls over the ice sheet, either because it directly contributes to the runoff flux, or because it increases the thermal energy of the snowpack. Since snowfall and runoff are the dominant terms in the mass budget, it can safely be concluded that melt will dominate changes in the mass balance of the Greenland ice sheet.

SU_s does not seem to be sensitive to temperature changes in winter, but is increased in spring. Raised temperatures allow for more sublimation when temperatures are still below freezing. In summer however, the rate of sublimation is increased because temperatures exceed the melting point and melt and evaporation occur instead. Interestingly, the variability at the end of summer increases strongly. SU_{ds} shows a decrease over all months except winter and early spring. Where it decreases, the reduction of TR_{ds} is dominant, while for the period of increase, higher sublimation rates in response to increased temperatures dominate.

5.2 Spatial patterns of change

While the above section considered only the seasonal cycle of certain variables, here the spatial patterns will be investigated to gain a more realistic understanding of the processes that cause the observed changes.

As before, the wind climate of the Greenland ice sheet is classified using the scale and shape parameter of the Weibull distribution. Figure 5.3 shows the annual average shape parameter for the two runs and the difference between them. The overall pattern of the scale parameter κ is unaltered. Low values are found in the south, where synoptic activity of passing cyclones is frequent, while high values are found in the north where katabatic forcing is strong and synoptic activity is weaker. Figure 5.3 clearly shows that κ is projected to decrease over the whole of Greenland, although changes in the south are extremely small. More intense synoptic activity, or reduced katabatic forcing are the most evident reasons that can cause this. Considering that the reduction is strongest in the north, it is likely that this reduction can be attributed to a reduced katabatic forcing rather than synoptic forcing.

Changes in the scale parameter are presented in Figure 5.4. Again, spatial patterns of both runs are nearly identical. The spatial pattern of change only becomes clear in the plot of the difference between the runs. A drop in the scale parameter is observed over most of the ice sheet, except at the edges. This drop of wind speed in the interior can either be caused by reduced synoptic forcing or by reduced katabatic forcing. The latter seems the most likely of the two, since a reduction of synoptic forcing is in direct contradiction with the reduced shape parameter over the same region. The distinct spatial pattern of the increase of the mean wind speed near the coast suggests that thermal forcing is responsible. This parameter is related to the horizontal gradient of the vertically integrated temperature deficit, which varies strongly over sloping terrain. To quantify these changes a full momentum budget analysis is performed in Section 5.3. Here the main analysis of changes in the Greenland climate is continued.

The temperature increase of 6 K over the ice sheet is clearly visible in Figure 5.5. A strong north-south gradient exists in the projected temperature rise. To the southeast of Greenland a moderate warming of 1 to 3 K is simulated, while the air to the north of Greenland warms by 7 K or more. Over the ice sheet, temperature rise ranges from 3 K in the southeast to over 6 K over the northern tundra and northerly parts of the ice sheet. The largest part of the ice sheet shows a remarkably uniform temperature increase of 5 to 6 K. The sensitivity of the north is likely related to changes in sea ice, although these were not explicitly investigated in this study. Since sea ice insulates the ocean, low temperatures are generally found over sea ice. A reduction in the length of sea ice duration or in the sea ice extent can therefore have large consequences for the near-surface temperature. Furthermore, apart from these local surface changes, a large-scale (Arctic region) signal of polar amplification will

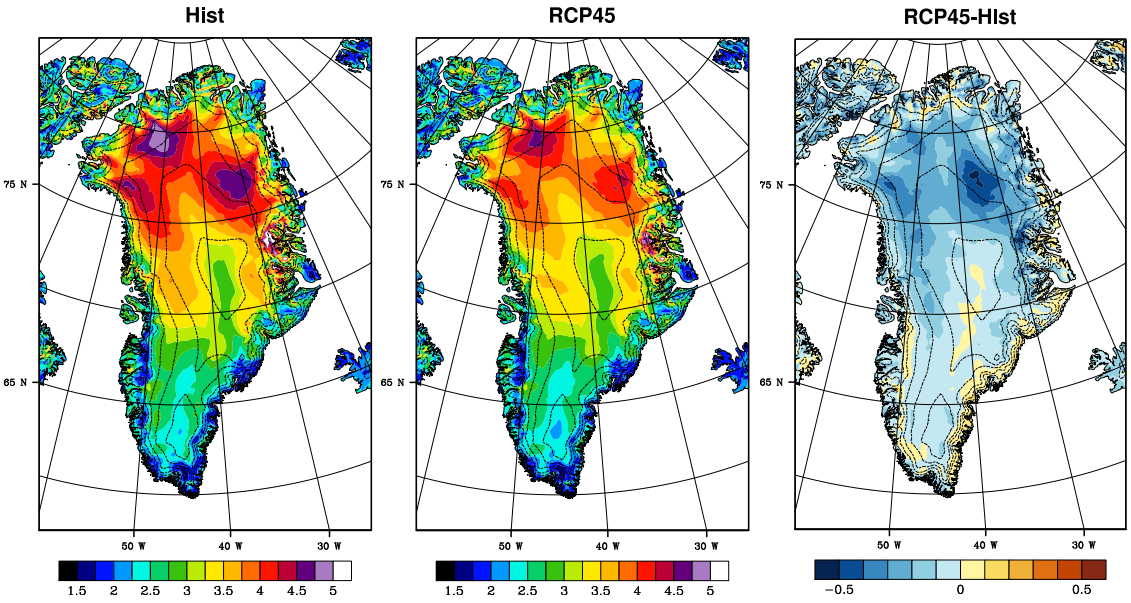

Figure 5.3: Map of the shape parameter κ (-) of the Weibull distribution for 1979-1998 (left), 2079-2098 (middle) and the difference (right).

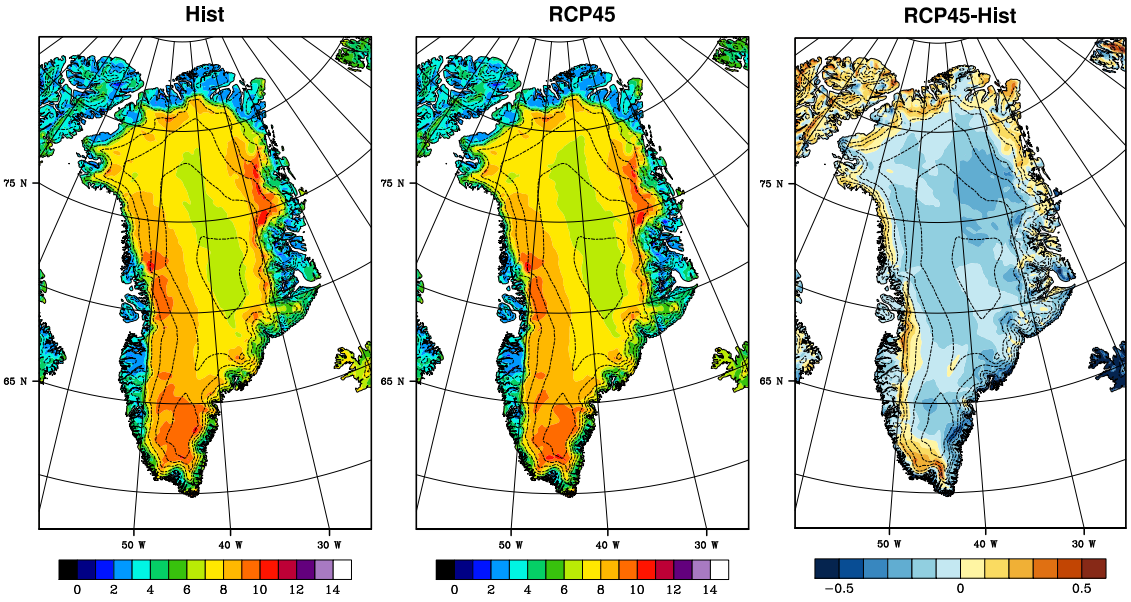

Figure 5.4: Map of the scale parameter λ (m s^{-1}) of the Weibull distribution for 1979-1998 (left), 2079-2098 (middle) and the difference (right).

further increase local temperature.

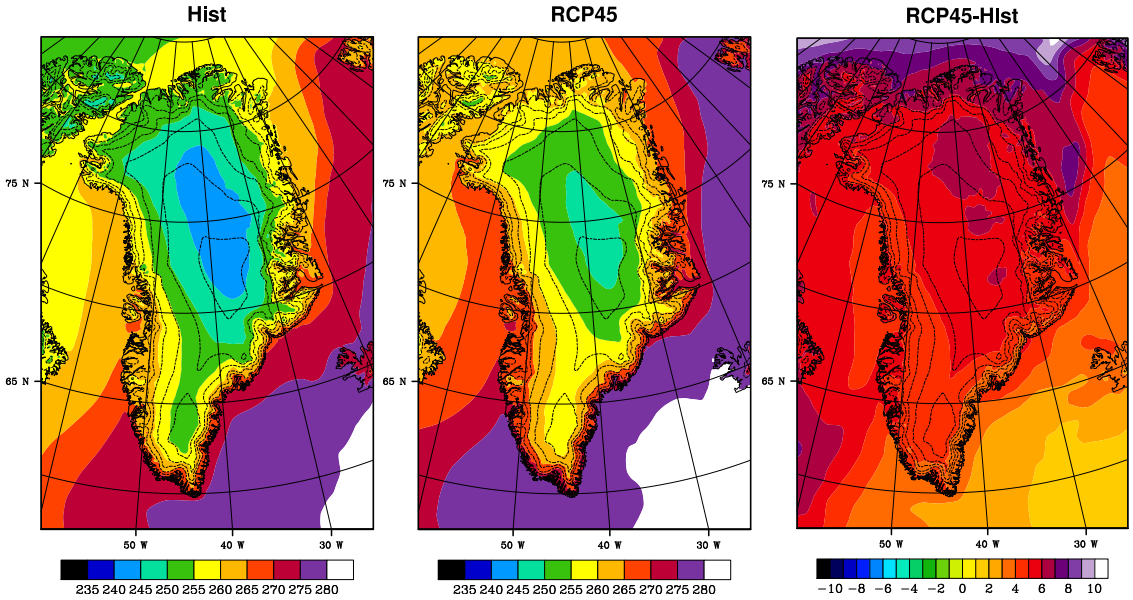

Figure 5.5: Map of 2m temperature (K) for 1979-1998 (left), 2079-2098 (middle) and the difference (right).

Precipitation changes show that snowfall increases everywhere on the ice sheet, except in the south in a narrow band at the coast. Here, precipitation is falling increasingly in the form of rain and snowfall therefore decreases. The pattern in the southeast nevertheless shows that the largest absolute snowfall increase is in that region. This should not be surprising considering that precipitation in that region is up to an order of magnitude larger than in the interior.

Figure 5.7 shows changes in snowdrift sublimation. Changes of SU_{ds} can be split in two contributions: in the warmer regions of the ice sheet along the western and southeastern coast, SU_{ds} decreases. In contrast, in the cold regions of the ice sheet, both at high elevations or in the north, snowdrift sublimation increases. This suggests that temperature is the controlling factor of these changes. Two processes occur in response to a temperature increase. First, the ambient thermal energy available for sublimation increases, such that sublimation of drifting snow is favored. Second, snow metamorphism and melt are increased, such that the threshold friction velocity increases and snowdrift is suppressed. In the warm regions, the latter argument appears to be dominant, such that snowdrift sublimation is reduced. In cold regions, temperatures are still well below the freezing point most of the season, and the increased thermal energy of the atmosphere will dominate the response. Since changes in snowdrift sublimation rates are of the order of 10% of the total value, and both negative and positive changes are observed, snowdrift sublimation will have a very limited impact on the change of the total surface mass balance of Greenland.

The projected changes in SU_s are of a slightly more complex nature. The pattern of change is similar to that of snowdrift sublimation in the sense that there is a clear distinction between the low lying coastal regions and the interior of the ice sheet. The RCP45 run projects that wintertime deposition in the coastal regions will become stronger. Deposition typically occurs under very cold conditions, and so not the projected temperature increase, but rather the associated increasing moisture content of the atmosphere is responsible for this change. The same argument likely applies to the interior of the ice sheet, but here the increase in summer sublimation dominates the signal and causes an increase in modeled mass loss. Changes in SU_s are larger than those in SU_{ds}, and are locally very large compared to the annual average sublimation. However, as for snowdrift sublimation, regions of

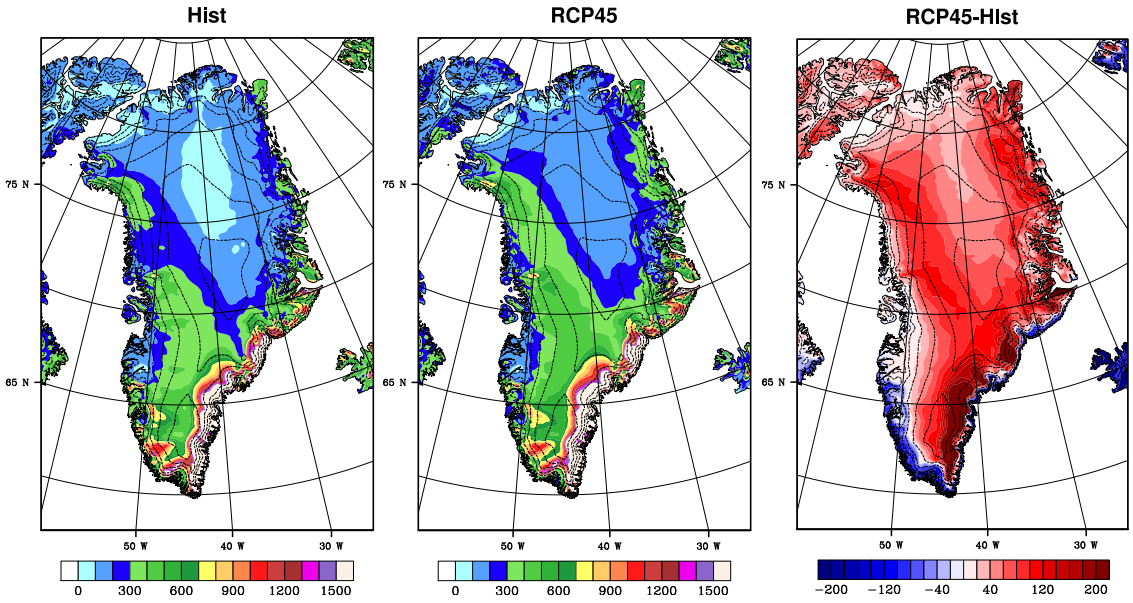

Figure 5.6: Map of snowfall (mm yr^{-1}) for 1979-1998 (left), 2079-2098 (middle) and the difference (right).

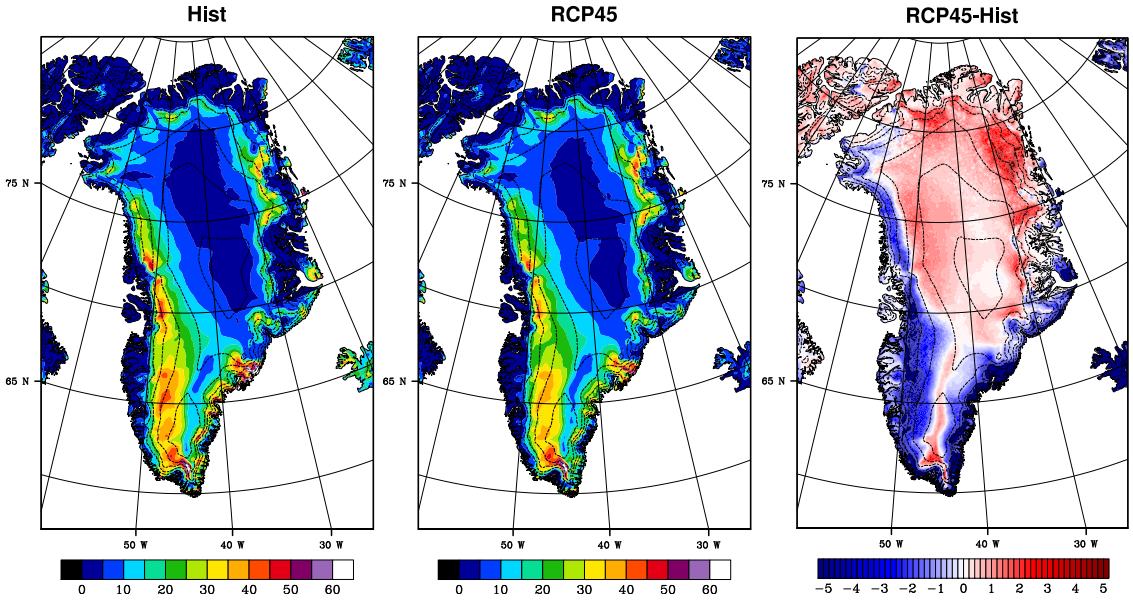

Figure 5.7: Map of snowdrift sublimation (mm yr^{-1}) for 1979-1998 (left), 2079-2098 (middle) and the difference (right).

positive and negative change limit the total effect on the ice sheet's surface mass balance, such that the total change is only 2 Gt yr^{-1}.

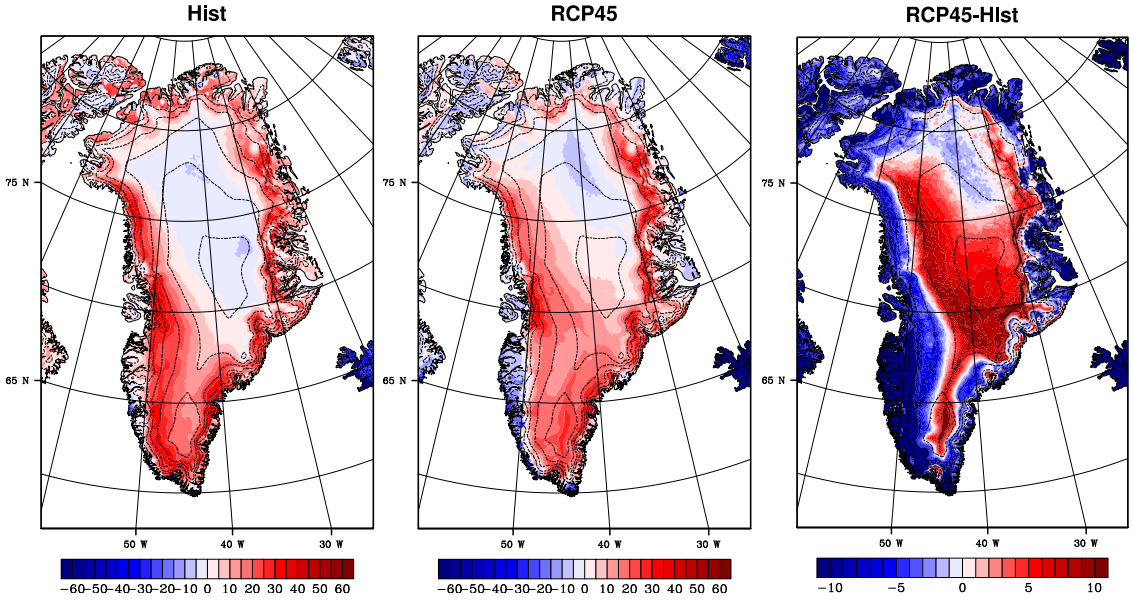

Figure 5.8: Map of surface sublimation (mm yr^{-1}) for 1979-1998 (left), 2079-2098 (middle) and the difference (right).

5.3 Changes in the momentum budget

Because the wind climate is of particular importance for the occurrence of snowdrift events, it is interesting to look in more detail at the processes that underly changes thereof. Section 5.2 showed the spatial patterns of change of the wind parameters. Here, the momentum budget is solved explicitly, with the exception of the advection terms, in an attempt to explain the projected changes. The procedure as laid out in Section 2.1 is used to solve for the individual components. Before considering changes of the momentum budget it is informative to show the spatial patterns of the forcing. In Figure 5.9 the induced acceleration due to the components LSC, THW and KAT is shown in colored contours. Furthermore, wind vectors are shown that represent the equivalent geostrophic wind, which is defined as the wind that would result if the shown forcing is balanced by the Coriolis acceleration. Most importantly, this neglects the effects of friction.

The large scale forcing prominently shows the Icelandic Low to the southeast of the ice sheet, which forces a cyclonic flow parallel to the coast in that region. Over the western parts of the ice sheet large scale forcing is relatively strong, in accordance with our earlier findings of a persistent southerly jet over this part of the ice sheet. LSC is relatively weak in the north, confirming the general picture that emerged from the spatial distribution of the shape parameter κ of the Weibull distribution, indicating that the northern part is less synoptically driven. Over the ocean along the western coastline, northerly winds are observed.

Thermal forcing is weak in the interior of the ice sheet. Here the surface slope is modest or small and the integrated potential temperature deficit is relatively low due to large scale subsidence, such that the horizontal gradients are weak. At the ice sheet margin, cold air drains on to the flat tundra where it builds up. This cold air pooling causes an increase in the height of the TDL and a strong thermal forcing. The direction of the equivalent geostrophic wind is difficult to see due to the complex

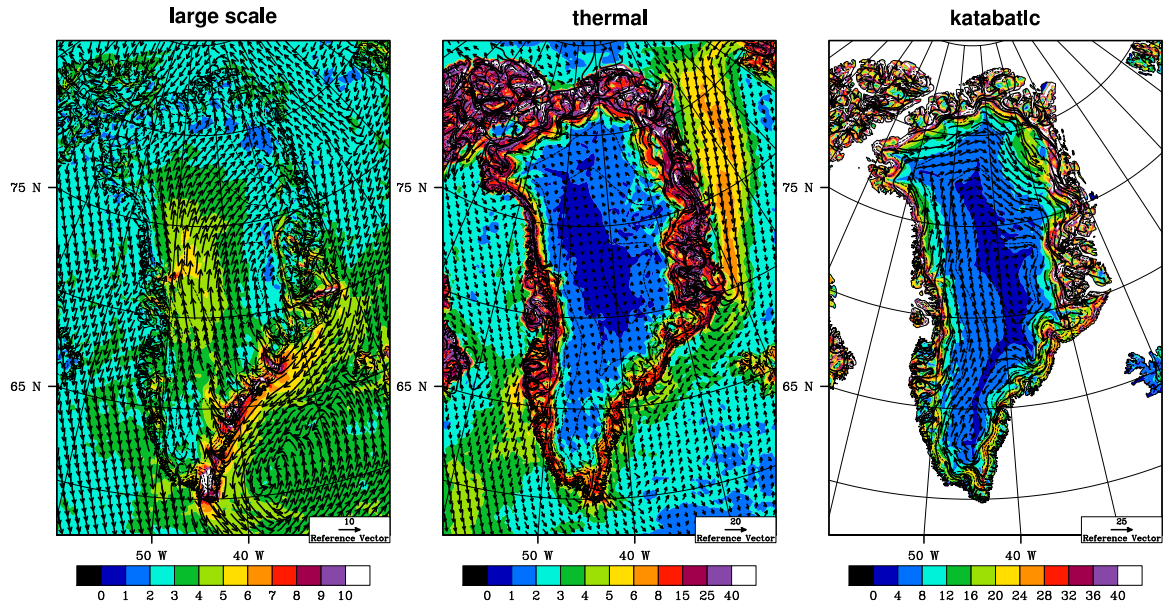

Figure 5.9: Map of annual average forcing terms of the momentum budget from 1981-1998. Colors and vectors indicate the strength and direction of the equivalent geostrophic wind (m s^{-1}) associated with the different forcings. Note the different scales.

topography over the tundra, but shows an cyclonic flow pattern over the ice sheet. Noteworthy is the flow over the sea ice region in the northeast. Here the ocean is insulated by the winter sea ice cover. In the absence of a surface slope cold air pooling is significant in this region. An outflow of cold air to the east creates an thermal pressure force to the east and corresponding southerly equivalent geostrophic winds. This nicely illustrates how THW forces southerly flow through Fram Strait and serves as major transport mechanism of sea ice into the Atlantic (Van Angelen et al., 2011).

Katabatic forcing is proportional to the surface slope and as such increases towards the ice sheet margin. On the plateau, KAT is of roughly equal magnitude as LSC. Towards the margins KAT quickly increases and is the dominant contribution over most of the peripheral ice sheet. The equivalent geostrophic wind shows an anti-cyclonic pattern, in contrast with THW. Over steep terrain, THW and KAT are often of similar magnitude and opposite direction, suggesting a relatively flat top of the TDL (Van den Broeke and Van Lipzig, 2003). The flow pattern induced by KAT strongly resembles the yearly average flow, confirming the dominant role of KAT in the Greenland wind climate.

To visualize the changes of all forcings, the December vertical profiles of all forcing terms are shown for both runs in Figure 5.10. These profiles are averages over the region of wind speed increase along the northeastern coast, as shown in Figure 5.4. The forcing in the x-direction is shown because at that location this roughly equals the downslope direction. For both runs, LSC is the dominant contribution above the atmospheric boundary layer, balanced by COR. Near the surface the effect of LSC is smaller, partly because the forcing is not directed in the downslope direction. The changing sign of LSC illustrates this directional dependence with height, driven by strong baroclinicity in this region (Van Angelen et al., 2011). Near the surface, the momentum budget is dominated by KAT and THW that represent strong opposing forces. In the interior, the influence of THW is strongly reduced due to the more gentle surface slope. The katabatic forcing is counteracted at the surface by the friction component, which quickly looses importance higher in the atmosphere. The result is a wind maximum at a few hundred meters above the surface. This is particularly well visible through the maximum of the COR and the changing sign of FDIV at a few hundred metres above the surface. Calculations

of FDIV as a residual (purple) and through a parameterization (yellow) are nearly indistinguishable, confirming the small influence of advection.

Changes in the momentum budget are dominated by a decrease in the thermal and katabatic forcing. Changes in the other forcing terms are small in comparison. The absence of large changes in the free troposphere suggests that the changes are driven by boundary layer processes. Since both forcings KAT and THW depend on the temperature deficit, it is expected that a significant reduction of the winter temperature deficit is responsible for the changes.

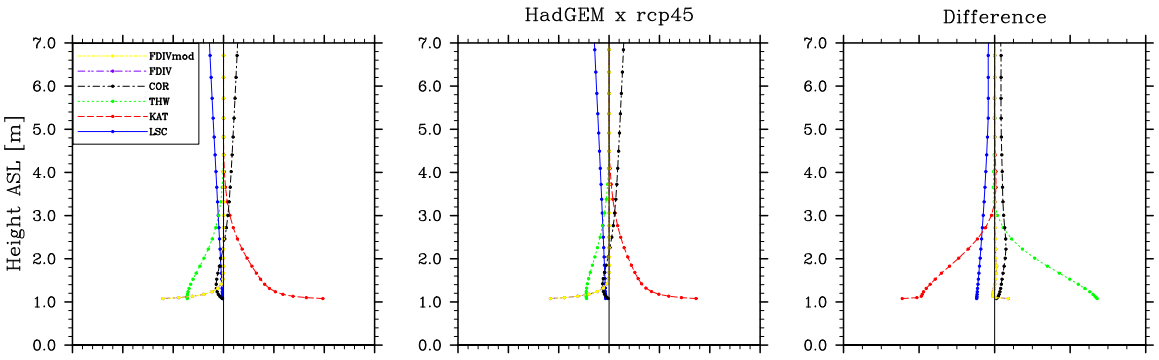

Figure 5.10: January x-direction momentum budget profiles for 1979-1998 (left), 2079-2098 (middle) and the difference between them (right).

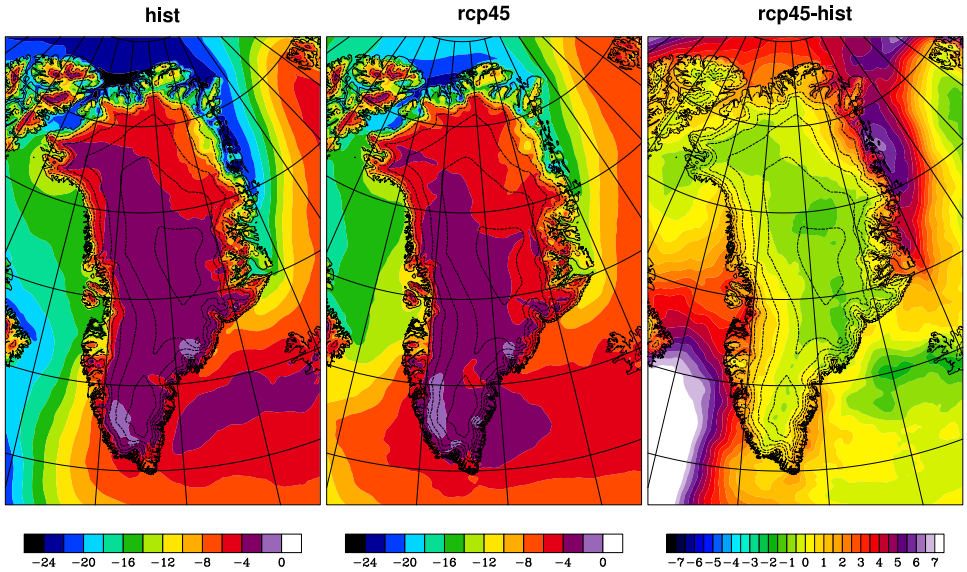

Figure 5.11: January integrated potential temperature deficit (10^3 K m).

Figure 5.11 shows the integrated January potential temperature deficit over the Greenland ice sheet and surrounding seas. Largest value of $\hat{\theta}$ are found to the north and northeast of the ice sheet over the tundra and adjacent sea ice. This is readily explained by the cold air pooling that occurs in those areas. Over the ice sheet the value of $\hat{\theta}$ is small, due to subsidence which limits the height of the

TDL. Over the ice sheet, differences in $\hat{\theta}$ are generally small, except near the ice edge and over the surrounding tundra. The most dramatic difference between the model runs is in the sea ice region to the northeast. Here, $\hat{\theta}$ is strongly reduced in response to a decline in sea ice extent, which shows as an increase (less negative) in the plot of the difference between the runs. Both the absolute value of the surface temperature deficit (not shown) and gradients of the vertically integrated deficit show a strong decline in the region, which confirms the results of Figure 5.10.

6 Discussion

In the previous two chapters, results were presented that describe the climate of the Greenland ice sheet, with particular attention for snowdrift processes. This chapter is meant to discuss the validity of the results where appropriate and to provide the necessary context to interpret these results. Weak elements of the analysis will be discussed, alternative data sources will be discussed and recommendations for future work are made.

The Automatic Weather Stations used in this study are extensively evaluated and known to produce reasonable values of the measured variables. However, two issues deserve some discussion. First, relative humidity values are corrected upward for low temperatures because they are outside the range of the detector calibration. When compared to model results, a negative model bias persists in winter, although this bias was improved by the inclusion of a snowdrift routine. The remaining bias could stem from inaccuracies of the model, or inaccuracies of the measurements correction. Since specific humidity and temperature are significantly better represented in RACMO2, and relative humidity is calculated from those, it is suggested that the model bias at least in part stems from inaccuracies in the measurement correction. Second, the time of operation of the three AWS is relatively short compared to timescales on which climate variability and change occurs. This hinders the ability to validate or detect decadal trends with the use of AWS data. As a consequence, it is essential that both model data and AWS data are used when studying trends.

Although regional climate models potentially yield data of unrivaled spatial and temporal coverage, they require validation against observations before gaining trustworthiness. RACMO2 was extensively evaluated and found to realistically simulate the Greenland climate. Nevertheless, improvements can be made. Two model assumptions that are relevant to the current project are highlighted here. First, the modeled wind climate depends strongly on the surface roughness length for momentum. Furthermore, the calculated turbulent fluxes depends crucially on the roughness lengths of heat and moisture. Few measurements of these roughness lengths exist, and usually a constant value is adopted. Yet detailed measurements in the southwestern ablation zone exist, but it is not clear whether these results are representative for other parts of the ice sheet (Smeets and van den Broeke, 2008). Secondly, the snowdrift parameterization adopted here is essentially a bulk non-spectral snowdrift routine. Instead of discretizing the particle size distribution it is described by an analytical function such as the gamma function. This function depends on three parameters, and therefore the particle evolution can be described by the evolution of these three parameters. The model adopted here allows only one of these variables to vary, such that vertically integrated sublimation is well represented, but not the vertical distribution of particles. Three-moment models now exist, which could improve results (Yang and Yau, 2008). Furthermore, the current model setup where column integrated fluxes of latent and sensible heat are released at the surface may be improved. Box et al. (2006) use a non-interactive snowdrift routine and note that the estimate of snowdrift sublimation they present depends on the snowdrift model chosen. However, they do not include feedbacks of snowdrift to the atmosphere and snow surface.

However, implementation of the above suggestions is perhaps not yet feasible, because no reliable measurements against which to compare the model results exist to date. Therefore, it is imperative that measurements of drifting snow processes on the Greenland ice sheet become available in order to allow for a quantitative assessment of model performance and model improvement. Field measurements of

snowdrift just above the equilibrium line in southwest Greenland are currently scheduled from August 2012 to summer or spring 2013 by IMAU/UU. Appendix A provides some further details.

Direct measurements of snowdrift also exist in the form of satellite measurements of the height of the blowing snow layer. However, prolonged snowdrift events longer than a few days are rare, and conditions are much less favorable to snowdrift than in Antarctica. Therefore, the blowing snow region is usually limited in size both horizontally and vertically, limiting the applicability of satellite data. Furthermore, clouds often tend to disturb measurements, limiting temporal and spatial coverage. In conclusion, though a valuable extra source of data, the satellite measurements cannot be expected to provide the amount of spatial and temporal detail on snowdrift events that is needed for model validation and quantitative estimates of SU_{ds}.

A final source of concern that deserves some discussion is the interpolation of free atmospheric temperature in the momentum budget calculation, that leads to the temperature deficit. Although qualitatively similar, the results (partly) presented here deviate sometimes substantially from results of Van Angelen et al. (2011). This is surprising, since it concerns output from the same model. Of course a small change in the fitted free tropospheric lapse rate yields rather large changes at the surface, which may explain the quantitative disagreement. For winter this explanation seems sufficient, considering the satisfactory qualitative agreement. In summer though, the approach pursued here yields very large values of the integrated temperature deficit over the oceans, in contradiction to intuition and results from Van Angelen et al. (2011). Therefore, the summer values were excluded from the analysis.

7 Conclusions

Using eight years of observations from automatic weather stations and 55 years of high resolution model simulations from the regional climate model RACMO2, the wind and snowdrift climate of the Greenland ice sheet is characterized. Furthermore, changes in the snowdrift climate in response to increasing atmospheric temperatures and increased radiative forcing are investigated. The model includes a new snow-albedo scheme that models the evolution of snow grains and an interactive drifting snow routine that accounts for the interaction between drifting snow, the atmosphere and the surface.

Detailed evaluation of AWS and RACMO2 data shows that the model is able to realistically simulate wind direction and wind speed, although it tends to slightly overestimate the low wind frequencies at the cost of the high wind frequencies. Biases are small, except near the edges of the ice sheet where topography or surface type may not be well represented in the model. In winter, a negative radiation balance cools the near surface air and drives an anti-cyclonic katabatic circulation that is typical of the large ice sheets. Because it depends linearly on the sine of the surface slope, the katabatically driven winds increase towards the ice sheet margin, where they reduce again in the ablation zone and particularly over the tundra in response to increasing surface roughness. The large scale circulation enhances the katabatic circulation. Over the steep slopes at the ice sheet margin thermal forcing represents a strong opposing force and counteracts the dominant circulation. The magnitude of both the synoptic and katabatic forcing decreases in summer resulting in lower wind speeds, although the synoptic forcing gains relative importance.

The two parameter Weibull distribution is fitted to the wind distribution to have a quantitative measure to characterize and compare the wind climate at different locations. Extremely uniform winds with high values of the shape parameter κ are found in regions of concave topography in the north, where katabatic winds show confluence. Lower values of the shape parameter, indicative of more important synoptic forcing, are found to the south. Values of the shape parameter are higher in winter because of the larger influence of the katabatic circulation. Values of the scale parameter λ closely follow the pattern of 10 m wind speed. Trends of these parameters are generally small, and longer time series are needed to statistically prove important patterns of change.

Temperature and specific humidity are well represented by the model, both in space and time. Relative humidity is realistically simulated by the model in summer, but the model unexpectedly shows a negative bias in winter. Possibly this is caused by the $\mathrm{RH_i}$ correction scheme that is used for the observations. Relative humidity generally decreases in the seaward direction, because it is reduced by adiabatic heating of the katabatic winds. From measurements, relative humidity is shown to increase significantly at high wind speeds, indicating the important role of snowdrift in describing the moisture budget over the ice sheet.

Because no reliable direct measurements of snowdrift are available on the Greenland ice sheet, it is currently not feasible to compare model results directly with observations. Instead, the snowdrift climate as obtained from the interactive snowdrift routine is presented *as is*, and the need for direct measurements is emphasized. Snowdrift is shown to be of little or no importance in summer, when melt increases the surface density and threshold friction velocity and when near-surface winds are weaker. In summer, ablation is dominated by runoff and to a lesser extent surface sublimation and evaporation, while snowdrift sublimation is not significant. In winter, melt is absent and surface sublimation typically turns into deposition, leaving drifting snow processes as the dominant contributor

of ablation. Drifting snow transport and frequency are highest in the northeast, south and western parts of the ice sheet, where high winds are found in combination with relatively low surface density. In the interior, the drifting snow processes are limited due to weaker winds. Integrated over the ice sheet, SU_{ds} equals 24 Gt yr^{-1}, and as such represents a small but significant contribution of 7% total ablation. Snowdrift sublimation is therefore 50% larger than surface sublimation, which is estimated at 16 Gt yr^{-1}. Snowdrift erosion due to divergence of the snowdrift transport flux is locally important as a redistributor of mass, but insignificant when integrated over the ice sheet.

To investigate changes of the Greenland wind and snowdrift climate, the model is forced with a scenario of moderate radiative forcing known as RCP4.5. Simulations with the general circulation model HadGEM2, forced with this scenario are used to force RACMO2 at the lateral boundaries. Comparison of model results from 1979-1998 with 2079-2098 reveals that the ice sheets responds to increased radiative forcing with an average temperature increase of 6 K. The temperature increase is larger in winter, because the surface temperature is limited to the melting point in summer. A small decrease in wind speed is observed, which is related to a decrease of the wintertime temperature deficit over the ice sheet and the katabatic winds it drives. This decrease in forcing is also captured by a reduction in the shape parameter of the Weibull distribution. Only in a small strip of land near the ice margin, winds increase due to counteracting effects of thermal and katabatic forcing. Melt is shown to be particularly sensitive to these changes, more than doubling in volume. Integrated over the ice sheet, snowdrift transport and frequency decline throughout the year, likely due to increased snow metamorphism which increases the threshold friction velocity. Snowdrift sublimation is not only linked to transport rates, but also to temperature and relative humidity. Because of this, SU_{ds} increases on the cold ice sheet plateau and in the north, where increased temperatures allow for larger sublimation rates. In coastal regions in the west and southeast, the snowdrift seasons is shortened and snow metamorphism dominates such that SU_{ds} decreases. Similarly, surface sublimation increases in the interior, while it decreases in the coastal regions due to increased melt and evaporation and increased winter deposition.

This thesis has characterized the wind and snowdrift climate of the Greenland ice sheet. It was shown that the wind climate is key to understand and describe the snowdrift climate. Signatures of snowdrift sublimation in observational data can be found, but no reliable measurements exist to date. The model result here presented therefore represents the first high-resolution regional climate modeling result to describe the Greenland snowdrift climate. This first attempt represents a *state of the art* analysis, but the scientific community is in dire need of snowdrift observations for future work.

Bibliography

Al-Fawzan, M. (2000). Methods for estimating the parameters of the Weibull distribution.

AMAP (2011). Snow, water, ice and permafrost in the Arctic (SWIPA): Climate change and the cryosphere. Technical report, Arctic Monitoring and Assessment Programme (AMAP), Oslo, Norway. xii + 538 pp.

Bamber, J., Layberry, R., and Gogineni, S. (2001). A new ice thickness and bed data set for the Greenland ice sheet: 1. measurement, data reduction, and errors. *Journal of Geophysical Research*, 106(D24):33,773–33,780.

Bigg, G. (1999). An estimate of the flux of iceberg calving from Greenland. *Arctic, Antarctic and Alpine Research*, 31(2):174–178.

Bintanja, R. (2000a). Snowdrift suspension and atmospheric turbulence. Part I: Theoretical background and model description. *Boundary Layer Meteorology*, 95(3):343–368.

Bintanja, R. (2000b). Snowdrift suspension and atmospheric turbulence. Part II: Results of model simulations. *Boundary Layer Meteorology*, 95(3):369–395.

Bintanja, R. (2001). Modelling snowdrift sublimation and its effect on the moisture budget of the atmospheric boundary layer. *Tellus A*, 53:215–232.

Bougamont, M., Bamber, J. L., and Greuell, W. (2005). A surface mass balance model for the Greenland ice sheet. *Journal of Geophysical Research*, 110(F04018).

Box, J. (2002). Survey of Greenland instrumental temperature records: 1873-2001. *Internaional Journal of Climatology*, 22:1829–1847.

Box, J., Bromwich, D., Veenhuis, B., Bai, L., Stroeve, J., Rogers, J., Steffen, K., Haran, T., and Wang, S. (2006). Greenland ice sheet surface mass balance variability (1988-2004) from calibrated Polar MM5 output. *Journal of Climate*, 19:27832800.

Box, J. and Cohen, A. (2006). Upper-air temperatures around Greenland: 1964-2005. *Geophysical Research Letters*, 33(L12706).

Box, J. and Decker, D. (2011). Greenland marine-terminating glacier area changes: 2000-2010. *Annals of Glaciology*, 52(59):91–98.

Box, J., Fettweis, X., Stroeve, J., Tedesco, M., Hall, D., and Steffen, K. (2012). Greenland ice sheet albedo feedback: thermodynamics and atmospheric drivers. *The Cryosphere Discuss*, 6:593–634.

Cappelen, J., Jørgensen, B., Laursen, E., Stannius, L., and Thomsen, R. (2001). The observed climate of Greenland, 1958-99 - with climatological standard normals, 1961-90. Technical Report 00-18, Danish Meteorological Institute, Ministery of Transport, Copenhagen, Denmark.

Comiso, J., Parkinson, C., Gersten, R., and Stock, L. (2008). Accelerated decline in the Arctic sea ice cover. *Geophysical Research Letters*, 35(L01703).

Curry, J. and Webster, P. (1999). *Thermodynamics of atmospheres and oceans*. Academic Press.

Déry, S. and Yau, M. (1999). A bulk blowing snow model. *Boundary Layer Meteorology*, 93:237–251.

Déry, S. and Yau, M. (2002). Large-scale mass balance efects of blowing snow and surface sublimation. *Journal of Geophysical Research*, 107(D23).

Dethloff, K., Schwager, M., Christensen, J., Kiilholm, S., Rinke, A., Dorn, W., Jung-Rothenhäusler, F., Fischer, H., Kipfstuhl, S., and Miller, H. (2002). Recent Greenland accumulation estimated from regional climate model simulations and ice core analysis. *Journal of Climate*, 15:2821–2832.

Doorschot, J., Lehning, M., and Vrouwe, A. (2004). Field measurements of snow-drift threshold and mass fluxes, and related model simulations. *Boundary-Layer Meteorology*, 113(3):347–368.

Ettema, J., van den Broeke, M., van Meijgaard, E., and van de Berg, W. (2010a). Climate of the Greenland ice sheet using a high-resolution climate model - Part 2: Near-surface climate and energy balance. *The Cryosphere*, 4:529–544.

Ettema, J., van den Broeke, M., van Meijgaard, E., van de Berg, W., Bamber, J., Box, J., and Bales, R. (2009). Higher surface mass balance of the Greenland ice sheet revealed by high-resolution climate modeling. *Geophysical Research Letters*, 36(L12501).

Ettema, J., van den Broeke, M., van Meijgaard, E., van de Berg, W., Box, J., and Steffen, K. (2010b). Climate of the Greenland ice sheet using a high-resolution climate model - Part 1: Evaluation. *The Cryosphere*, 4:511–527.

Fettweis, X. (2007). Reconstruction of the 19792006 Greenland ice sheet surface mass balance using the regional climate model MAR. *The Cryosphere*, 1:21–40.

Gallée, H., Guyomarc'h, G., and Brun, E. (2001). Impact of snow drift on the Antarctic ice shet surface mass balance: possible sensitivity to snow-surface properties. *Boundary Layer Meteorology*, 99:1–19.

Garratt, J. (1994). *The atmospheric boundary layer*. Cambridge atmospheric and space science series. Cambridge University Press. ISBN 9780521467452.

Gregory, J. and Huybrechts, P. (2006). Ice-sheet contributions to future sea-level change. *Philosophical Transactions of the Royal Society A-Mathematical Physical and Engineering Sciences*, 364(1844):1709–1731.

Hanna, E., Huybrechts, P., Janssens, I., Cappelen, J., Steffen, K., and Stephens, A. (2005). Runoff and mass balance of the Greenland ice sheet: 1958-2003. *Journal of Geophysical Research*, 110(D13108).

Hanna, E., Huybrechts, P., Steffen, K., Cappelen, J., Huff, R., Shuman, C., Irvine-Fynn, T., Wise, S., and Griffiths, M. (2008). Inreased runoff from melt from the Greenland ice sheet: a response to global warming. *Journal of Climate*, 21:331–341.

Hansen, J., Ruedy, R., Sato, M., and Lo, K. (2010). Global surface temperature change. *Reviews of Geophysics*, 48(RG4004).

Heinemann, G. (1999). The KABEG'97 field experiment: an aircraft-based study of katabaticwind dynamics over the Greenland ice sheet. *Boundary Layer Meteorology*, 93:75–116.

Holland, D., Thomas, R., de Young, B., Ribergaard, M., and Lyberth, B. (2008). Acceleration of Jakobshavn Isbræ triggered by warm subsurface ocean waters. *Nature Geoscience*, 1:659–664.

Kuipers Munneke, P., van den Broeke, M., Lenaerts, J., Flanner, M., Gardner, A., and van de Berg, W. (2011). A new albedo parameterization for use in climate models over the Antarctic ice sheet. *Journal of Geophysical Research*, 116(D05114).

Lenaerts, J. and van den Broeke, M. (2012). Modelling drifting snow in Antarctica with a regional climate model: Part 2. Results. *Journal of Geophysical Research*, 117(DD05109).

Lenaerts, J., van den Broeke, M., Dry, S., Knig-Langlo, G., Ettema, J., and Munneke, P. (2010). Modelling snowdrift sublimation on an Antarctic ice shelf. *The Cryosphere*, 4:179–190.

Lenaerts, J., van den Broeke, M., Dry, S., van Meijgaard, E., van de Berg, W., Palm, S., and Sanz Rodrigo, J. (2012a). Regional climate modelling of drifting snow in Antarctica, Part I: methods and model evaluation. *Journal of Geophysical Research*, 117(D05108).

Lenaerts, J., van den Broeke, M., van Angelen, J., van Meijgaard, E., and Dry, S. (2012b). Drifting snow climate of the Greenland ice sheet: a study with a regional climate model. *The Cryosphere Discussions*, 6:1611–1635.

Ligtenberg, S., Helsen, M., and van den Broeke, M. (2011). An improved semi-empirical model for the densification of Antarctic firn. *The Cryosphere*, 5:809–819.

Lu, H., Chen, C., and Wu, J. (2004). A note on weighted least squares estimation of the shape parameter of the Weibull distribution. *Quality and Reliability Engineering International*, 20:579,586.

Mann, G., Anderson, P., and Mobbs, S. (2000). Profile measurements of blowing snow at Halley, Antarctica. *Journal of Geophysical Research*, 105(D19):24491–24508.

Moon, T. and Joughin, I. (2008). Changes in ice front position on Greenland's outlet glaciers from 1992 to 2008. *Journal of Geophysical Research - Earth Surface*, 113(F02022).

Moss, R., Babiker, M., Brinkman, S., Calvo, E., Carter, T., Edmonds, J., Elgizouli, I., Emori, S., Erda, L., Hibbard, K., Jones, R., Kainuma, M., Kelleher, J., Lamarque, J. F., Manning, M., Matthews, B., Meehl, J., Meyer, L., Mitchell, J., Nakicenovic, N., ONeill, B., Pichs, R., Riahi, K., Rose, S., Runci, P., Stouffer, R., van Vuuren, D., Weyant, J., Wilbanks, T., van Ypersele, J. P., and Zurek, M. (2008). Towards new scenarios for analysis of emissions, Climate Change, Impacts and Response Strategies. Techical summary, Intergovernmental Panel on Climate Change.

Oerlemans, J. (2005). Extracting a climate signal from 169 glacier records. *Science*, 308:675–677.

Oerlemans, J., Bassford, R., Chapman, W., Dowdeswell, J., Glazovsky, A., Hagen, J.-O., Melvold, K., de Ruyter de Wildt, M., and van de Wal, R. (2005). Estimating the contribution of Arctic glaciers to sea-level change in the next 100 years. *Annals of Glaciology*, 42:230–236.

Oerlemans, J. and Vugts, H. (1993). A meteorological experiment in the melting zone of the Greenland ice sheet. *Bulletin of the American Meteorological Society*, 74(3):355–365.

Palm, S., Yang, Y., Spinhirne, J., and Marshak, A. (2011). Satellite remote sensing of blowing snow properties over Antarctica. *Journal of Geophysical Research*, 116(D16123).

Reeh, N. (1994). Calving from greenland glaciers: Observations, balance estimates of calving rates, calving laws. In *Report of a Workshop on the Calving Rate of West Greenland Glaciers in Response to Climate Change*, pages 85–102, Danish Polar Center, Copenhagen.

Rignot, E., Box, J., Burgess, E., and Hanna, E. (2008). Mass balance of the Greenland ice sheet from 1958 to 2007. *Geophysical Research Letters*, 35(L20502).

Rignot, E. and Kanagaratnam, P. (2006). Changes in the velocity structure of the Greenland ice sheet. *Science*, 311:986–990.

Rignot, E., Velicogna, I., van den Broeke, M., Monaghan, A., and Lenaerts, J. (2011). Acceleration of the contribution of the Greenland and Antarctic ice sheets to sea level rise. *Geophysical Research Letters*, 38(L05503).

Rodrigo, J. S., van Beeck, J., Buchlin, J., Lenaerts, J., and van den Broeke, M. (2012). Evaluation of Antarctic surface winds from ERA Reanalyses and RACMO/ANT mesoscale simulations based on Automatic Weather Stations. Accepted for publication in Climate Dynamics.

Santer, B., Wigley, T., Boyle, J., Gaffen, D., Hnilo, J., Nychka, D., Parker, D., and Taylor, K. (2000). Statistical significance of trends and trend differences in layer-average atmospheric temperature time series. *Journal of Geophysical Research*, 105(D6):7337–7356.

Schmidt, R. (1986). Transport rate of drifting snow and the mean wind speed profile. *Boundary-Layer Meteorology*, 34(3):213–241.

Slangen, A., Katsman, C., van de Wal, R., Vermeersen, L., and Riva, R. (2012). Towards regional projections of twenty-first century sea-level change based on IPCC SRES scenarios. *Climate Dynamics*, 38:1191–1209.

Smeets, C. and van den Broeke, M. (2008). Temporal and spatial variations of the aerodynamic roughness length in the ablation zone of the Greenland ice sheet. *Boundary-Layer Meteorology*, 128(3):315–338.

Steffen, K. and Box, J. (2001). Surface climatology of the Greenland ice sheet: Greenland Climate Network 1995-1999. *Journal of Geophysical Research*, 106(D24):33.951–33.964.

Undén, P., Rontu, L., Järvinen, H., Lynch, P., Calvo, J., Cats, G., Cuxart, J., Eerola, K., Fortelius, C., Garcia-Moya, J. A., Jones, C., Lenderlink, G., Mcdonald, A., Mcgrath, R., Navascues, B., Nielsen, N. W., Ødegaard, V., Rodriguez, E., Rummukainen, M., Rõõm, R., Sattler, K., Sass, B. H., Savijärvi, H., Schreur, B. W., Sigg, R., The, H., and Tijm, A. (2002). HIRLAM-5 scientific documentation. Technical report, Swedish Meteorological and Hydrological Institute, Norrköping, Sweden.

Van Angelen, J., Lenaerts, J., Lhermitte, S., Fettweis, X., Kuipers Munneke, P., Van den Broeke, M., and Van Meijgaard, E. (2012). Sensitivity of Greenland ice sheet surface mass balance to surface albedo parameterization: a study with a regional climate model. *The Cryosphere Discuss*, 6:1531–1562.

Van Angelen, J., Van den Broeke, M., and Van de Berg, W. (2011). Momentum budget of the atmospheric boundary layer over the Greenland ice sheet and its surrounding seas. *Journal of Geophysical Research*, 116(D10101).

Van As, D., Fausto, R., and project team, P. (2011). Programme for monitoring of the Greenland ice sheet (PROMICE): first temperature and ablation recors. *Geological Survey of Denmark and Greenland Bulletin*, 23:73–76.

Van de Wal, R., Greuell, W., Van den Broeke, M., Reijmer, C., and Oerlemans, J. (2005). Surface mass-balance observations and automatic weather station data along a transect near Kangerlussuaq, West Greenland. *Annals of Glaciology*, pages 311–316.

Van den Broeke, M., Bamber, J., Ettema, J., Rignot, E., Schrama, E., Van de Berg, W., Van Meijgaard, E., Velicogna, I., and Wouters, B. (2009). Partitioning recent Greenland mass loss. *Science*, 326:984–986.

Van den Broeke, M., Duynkerke, P., and Oerlemans, J. (1994). The observed katabatic flow at the edge of the Greenland ice sheet during GIMEX-91. *Global and Planetary Change*, 9:3–15.

Van den Broeke, M., Reijmer, C., and Van de Wal, R. (2004). A study of the surface mass balance in Dronning Maud Land, Antarctica, using automatic weather stations. *Journal of Glaciology*, 50(171):565–582.

Van den Broeke, M., Smeets, P., Ettema, J., and Kuipers Munneke, P. (2008a). Surface radiation balance in the ablation zone of the west Greenland ice sheet. *Journal of Geophysical Research*, 113(D13105).

Van den Broeke, M., Smeets, P., Ettema, J., Van der Veen, C., Van de Wal, R., and Oerlemans, J. (2008b). Partitioning of melt energy and meltwater fluxes in the ablation zone of the west Greenland ice sheet. *The Cryosphere*, 2(2):179–189.

Van den Broeke, M. and Van Lipzig, N. (2003). Factors controlling the near-surface wind field in Antarctica. *Monthly Weather Review*, 131:733–743.

Van Meijgaard, E., Van Ulft, L., Van de Berg, W., Bosveld, F., Van den Hurk, B., Lenderink, G., and Siebesma, A. (2008). The KNMI regional atmospheric climate model RACMO version 2.1. Technical Report TR - 302, Royal Netherlands Meteorological Institute, De Bilt, the Netherlands.

White, P. (2001). Physical processes (CY23R4). Technical report, European Centre for Medium-Range Weather Forecasts (ECMWF).

Xiao, J., Bintanja, R., Déry, S., Mann, G., and Taylor, P. (2000). An intercomparison among four models of blowing snow. *Boundary Layer Meteorology*, 97(1):109–135.

Yang, J. and Yau, M. (2008). A new triple-moment blowing snow model. *Boundary-Layer Meteorology*, 126(1):137–155.

Zwiers, F. and von Storch, H. (1995). Taking serial correlation into account in tests of the mean. *Journal of Climate*, 8:336–351.

Appendix A: Field Campaign

In the above, the need for direct reliable observations of snowdrift was stressed on numerous occasions. To overcome this shortage of observations, a field campaign from IMAU/UU is scheduled in August 2012 to install a measurements device just above the equilibrium line in the southwest of the Greenland ice sheet. This section is meant as a very short non-technical overview of these activities.

Figure 7.1 shows the setup of the device in a test setting in the Netherlands. The device consists of a profile mast 8 meters high (left mast), which is equipped with wind, humidity and temperature sensors, at various heights. Furthermore, it is equipped with a sonic anemometer to measure the turbulent fluxes. This setup allows for very detailed profiles of temperature, humidity and wind speed and direction.

The device further contains two direct sensors for the detection of snowdrift, which essentially serve as particle counters. These are positioned at 0.5m and 1m height, and kept at that height above the surface during the year. These are a little difficult to see, but are attached to the frame between the left and middle mast.

The whole setup is powered by two wind-generators that will provide the required energy. These are found at two different altitudes to ensure that both receive sufficient wind power, regardless of wind direction.

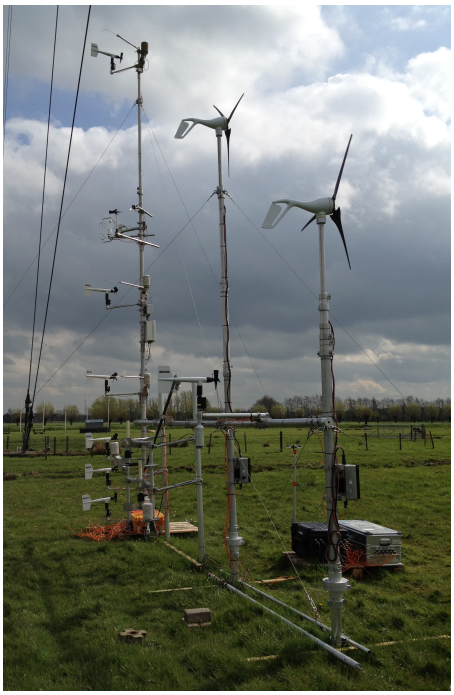

Figure 7.1: Snowdrift measurement setup at a test location in Cabauw.